Seismic velocity anisotropy and heterogeneity beneath the Mantle Electromagnetic and Tomography Experiment (MELT) region of the East Pacific Rise from analysis of *P* and *S* body waves

William C. Hammond[1] and Douglas R. Toomey

Department of Geological Sciences, University of Oregon, Eugene, Oregon, USA

[1]   We use teleseismic *P* and *S* delay times and shear wave splitting measurements to constrain isotropic and anisotropic heterogeneity in the mantle beneath the southern East Pacific Rise (SEPR). The data comprise 462 *P* and *S* delay times and 18 shear wave splitting observations recorded during the Mantle Electromagnetic and Tomography (MELT) Experiment. We estimate the mantle melt content (F) and temperature (T) variation from the isotropic velocity variation. Our results indicate that the maximum variation in F beneath our array is between zero and ~1.2%, and maximum variation in T is between zero and ~100 K. We favor an explanation having partial contributions from both T and F. We approximate the seismic anisotropy of the upper mantle with hexagonal symmetry, consistent with the assumption of two dimensionality of mantle flow. Our new tomographic technique uses a nonlinear inversion of *P* and slow *S* polarization delay times to simultaneously solve for coupled V_P and V_S heterogeneity throughout the model and for the magnitude of anisotropy within discrete domains. The domain dimensions and the dip of the anisotropy are fixed for each inversion but are varied in a grid search, obtaining the misfit of the models to the body wave delay data and to split times of vertically propagating *S* waves. The data misfit and the isotropic heterogeneity are sensitive to domain dimensions and dip of anisotropy. In a region centered beneath the SEPR the best average dip of the hexagonal symmetry axis is horizontal or dipping shallowly (<30°) west. Given the resolution of our data, a subaxial region characterized by vertically aligned symmetry axes may exist but is limited to be <80 km deep. We infer that the mantle flow beneath the SEPR is consistent with shallow asthenospheric return flow from the direction of the South Pacific superswell.   *INDEX TERMS:* 1025 Geochemistry: Composition of the mantle; 3025 Marine Geology and Geophysics: Marine seismics (0935); 3035 Marine Geology and Geophysics: Midocean ridge processes; 7218 Seismology: Lithosphere and upper mantle; 8121 Tectonophysics: Dynamics, convection currents and mantle plumes; *KEYWORDS:* mantle flow, melt generation, mid-ocean ridge, seismic tomography, seismic anisotropy, East Pacific Rise

1. Introduction

[2]   The forces that drive upwelling in the mantle beneath a mid-ocean ridge can be classified into two groups, as viscous tractions exerted by the movement of the overlying diverging plates, or as buoyancy forces supplied by density variations owing to pressure release partial melting of the ascending peridotite. In the absence of influences external to the ridge, some combination of these forces control the pattern of upper mantle flow. Understanding the relative importance of these mechanisms is equivalent to determining if the flow is a passive (viscous) response to plate motions, or if there is an active (buoyant) or plate-independent component of upwelling. In one model, "active" flow has been associated with melt concentrated in a narrow zone beneath the rise with a strongly focused vertical upwelling [*Buck and Su*, 1989; *Su and Buck*, 1991]. Alternatively, if the melt is broadly distributed, then a wider flow pattern is expected [*Scott and Stevenson*, 1989; *Turcotte and Phipps Morgan*, 1992]. Thus the melt distribution is seen as a signature of the dominant dynamics of subridge mantle flow.

[3]   The Mantle ELectromagnetic and Tomography (MELT) Experiment was designed to investigate this and other questions about the nature of mantle flow and melt

---

[1]Now at U.S. Geological Survey, Menlo Park, California, USA.

generation beneath the superfast spreading southern East Pacific Rise (SEPR). The experiment addressed a critical unknown: is the pattern of mantle flow a broad and passive response to plate divergence, or is it characterized by buoyant and narrowly focused upwelling beneath the rise [*MELT Seismic Team*, 1998]. Our primary goal in this study is to constrain the seismic structure and geometry of mantle flow by using teleseismic body waves recorded by the MELT seismic array. Using seismic tomography we obtain constraints on the distribution of seismic velocity anomalies that constrain models of upwelling. We must consider that the presence of melt or elevated temperature reduces seismic velocities [*Mavko*, 1980; *Schmeling*, 1985; *Sato et al.*, 1988; *Hammond and Humphreys*, 2000], and that the presence of a preferred orientation of olivine crystals owing to shear strain causes a strong seismic anisotropy [e.g., *Hess*, 1964; *Raitt et al.*, 1969; *Keen and Barrett*, 1971; *Forsyth*, 1975; *Nicolas and Christensen*, 1987; *Babuska and Cara*, 1991; *Ribe and Yu*, 1991; *Zhang and Karato*, 1995]. The magnitude of the signal owing to anisotropy at a mid-ocean ridge can be a significant component of the entire body wave delay time signal [*Kendall*, 1994; *Blackman et al.*, 1996; *Blackman and Kendall*, 1997]. To address this issue, we solve for both the distribution of isotropic (i.e., directionally averaged) seismic velocity variation and for anisotropy in wave velocity.

[4] We use the complementary resolving strengths of *P* and *S* wave delay times and shear wave splitting measurements to constrain mantle structure. The body wave delay times are sensitive to isotropic velocity variations as well as anisotropy, while shear wave splitting is mostly sensitive to anisotropy. To determine the seismic velocity structure we use an enhanced tomographic method that simultaneously inverts *P* and *S* delay times. For each tomographic inversion we fix the pattern of hexagonally symmetric anisotropy a priori, and solve for the isotropic heterogeneity and the magnitude of the anisotropy. Then dimensions of the a priori anisotropic region are varied systematically, providing a relation between the pattern of anisotropy and data misfit. Predicted shear wave splitting delay times are compared to the splitting measurements made by *Wolfe and Solomon* [1998], allowing the elimination of some models from consideration. We find that the data favor models with anisotropic symmetry axes dipping shallowly to the west. The data can eliminate models having vertically oriented symmetry axes penetrating more deeply than ∼80 km. The region of lowest seismic velocities penetrates to >200 km in depth.

2.   Background: The MELT Experiment

[5] The MELT experiment [*MELT Seismic Team*, 1998] was conducted along the superfast spreading (145 mm/yr) SEPR near 17°S (Figure 1). The site lies within a section of the SEPR, between 0° and 30°S, that accounts for >20% of the Earth's annual budget of plate creation, an amount exceeding that of the Mid-Atlantic and southwest Indian Ridges combined. In the vicinity of the MELT site, the rise axis is continuous for over 800 km, making it the longest section of the global ridge system that is uninterrupted by transform faults. Given the fast spreading rate and the relatively uniform axial morphology, this section of the rise

is thought to have a two-dimensional structure [*Parmentier and Phipps Morgan*, 1990]. The MELT experiment was thus designed to image primarily cross-axis variations in mantle properties. The MELT seismic array therefore comprised two cross-axis lines of ocean bottom seismometers (OBSs) connected by a smaller line located near the rise axis. The 800 km long cross-axis arrays were oriented to maximize aperture with respect to teleseismic sources in the western Pacific subduction zones, while also being as perpendicular to the SEPR as possible. The southern cross-axis (primary) array was deployed near an along-axis topographic high characterized by a broad axial summit. The northern (secondary) array was deployed just northward of a small offset overlapping spreading center. All OBSs were deployed for ∼6 months.

[6] In combination with earlier studies, the MELT experiment revealed asymmetries in structure that extend from the seafloor into the upper mantle. The region west of the rise, relative to the east, is characterized by faster absolute plate motion, slower seafloor subsidence [*Cochran*, 1986], more abundant seamounts, less dense mantle [*Scheirer et al.*, 1998], greater shear wave splitting [*Wolfe and Solomon*, 1998], lower seismic velocities, [*Forsyth et al.*, 1998; *Toomey et al.*, 1998], and higher electrical conductivity [*Evans et al.*, 1999]. With nearly symmetric spreading, faster motion of the Pacific plate forces the spreading center to migrate rapidly westward. In contrast to the above asymmetries, the crustal thickness is relatively uniform to either side of the rise [*Canales et al.*, 1998]. Also, at deeper depths, there is no resolvable deflection in the upper mantle discontinuities near the rise, nor any east-to-west asymmetry in their depths [*Shen et al.*, 1998].

[7] Observations from the MELT experiment indicate that upper mantle seismic anisotropy is laterally variable. On the basis of shear wave splitting results, *Wolfe and Solomon* [1998] demonstrated that while the direction of fast shear wave polarization was consistently parallel to the spreading direction, the delay times between fast and slow shear waves on the Pacific plate were twice those on the Nazca plate. These results were interpreted as evidence for a thicker layer of anisotropic material beneath the Pacific plate. *Toomey et al.* [1998] interpreted a gradual decrease in *P* delays within ±100 km of the rise as consistent with the subvertical alignment of the crystallographic *a* axis of olivine crystals in an upwelling region with a half width of less than 100 km. From the inversion of Rayleigh waves, *Forsyth et al.* [1998] infer that the degree of azimuthal anisotropy decreases in the vicinity of the rise, consistent with more vertically aligned olivine, or with a lesser magnitude of anisotropy owing to a melt-induced shift from the anisotropy-producing dislocation creep to the anisotropy-destroying diffusion creep deformation mechanism [*Karato and Wu*, 1993]. Seismic anisotropy, if unaccounted for, can thus give rise to artifacts in tomographic images and obscure the signals from anomalous temperature or partial melt [*Blackman et al.*, 1996; *Blackman and Kendall*, 1997].

[8] Previously, we presented the delay times of *P* and *S* body waves and the results of tomographic inversions for isotropic heterogeneity [*Toomey et al.*, 1998]. We showed that a broad zone of low seismic velocities extends beneath the rise to depths of about 200 km and is centered to the
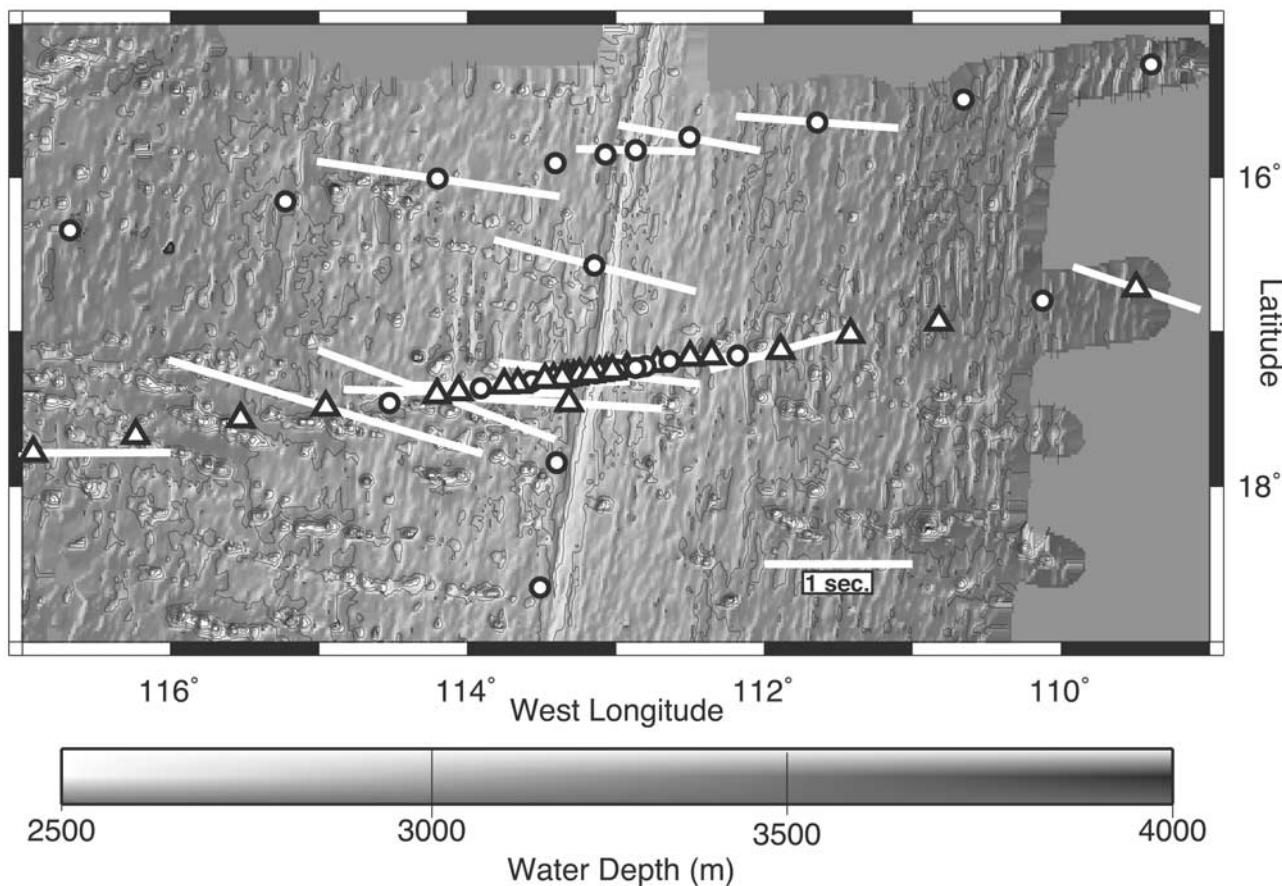
Figure 1. Bathymetric map of the southern East Pacific Rise with the locations of ocean bottom seismometers (circles and triangles) deployed during the MELT experiment. Current analysis uses data from a subset of OBSs (triangles) deployed along the primary array. Shear wave splitting measurements of *Wolfe and Solomon* [1998] are indicated by solid black lines; orientation and length of line represents fast polarization direction and split time, respectively.

west of the rise. We did not attempt to account for the effects of seismic anisotropy in that study, nor did we formally couple the independent P and S wave delay time data. Here we use an expanded set of delay time data to constrain anisotropic models of coupled P and S wave velocity beneath the primary seismic array. We use the shear wave splitting results of *Wolfe and Solomon* [1998], to constrain the pattern of anisotropy in our starting models, so that the final result will be consistent with the body wave data.

3. Body Wave Delay Time Data

[9] The 22 teleseismic events used in this analysis have a broad distribution of back azimuths and angles of incidence (Figure 2), providing good crossing ray coverage of the upper mantle beneath the array. Events most commonly originate from the circum-Pacific subduction zones, having epicentral distances of 28° to 113°, providing angles of incidence in the mantle beneath the array between 10° and 35° (Table 1). For the tomographic analysis we used 26 stations from the primary array from which high quality delay times were derived. Body wave delay times were identified on the horizontal and vertical seismometer chan-

nels and differential pressure gauges (DPG) (Figure 1). In total, 303 P and 159 S delays were measured.

[10] Prior to measuring delay times all seismograms were corrected for instrument response and band pass filtered. Transfer functions describing instrument response were provided by the OBS groups http://www-mpl.ucsd.edu/obs/reports/tn061). To each trace, we applied a four-pole, Butterworth filter forward and backward to provide a zero phase response with corner periods of 12 and 33 s, equivalent to wavelengths of $\sim$100–250 (50–130) km for P (S) waves in the mantle. In this band, the signal-to-noise ratio is highest since it coincides with a notch in the microseism noise spectrum [*Webb*, 1998; *Wilcock and Webb*, 1999]. P and SV wave delay times were measured on the vertical component seismometers and DPGs. The use of DPG data significantly improves spatial coverage, thereby better defining near-axis delay time trends. By using periods in excess of the four-way, vertical travel time in the water column, we avoid the adverse effects of water column reverberations on the DPG waveforms [*Blackman et al.*, 1995]. Empirical transfer functions that convert DPG waveform data to vertical component seismometer data were obtained from the MELT data (D. Forsyth, personal communication, 2000). For the period band of 12 to 33 s,

Figure 2. Distribution of events used in the tomographic analysis. Location of MELT experiment shown by triangle. The great circle path between an event and the array is shown by an arcuate line. Symbols at source end of path indicates phase observed from the event: *P* only (open square), *S* only (open circle), or both *P* and *S* (solid circle).

the delays measured at sites which recorded both seismometer and DPG data were in excellent agreement, i.e., no discernible difference between vertical component seismometer and transformed DPG waveforms was found. Example seismograms are shown in Figure 3. The similarity in the details of the waveforms indicate that the vertical and

DPG responses have been correctly normalized. The P wave delay times measured from the seismometers at shorter periods (2–7 s) [*Toomey et al.*, 1998, Figure 1] have similar patterns as the longer period delays reported here.

[11] Shear wave delay times were measured from phases consistent with particle motion in the anisotropically slow polarization direction (Appendix A). Earlier measurement of the anisotropy of the SEPR showed that the faster polarization and propagation direction is roughly parallel to the direction of plate motion [*Forsyth et al.*, 1998; *Wolfe and Solomon*, 1998]. Hence for events with ray path back azimuths within 14° of the strike of the SEPR, we obtained delay times from the vertical component seismometer and DPG channels. Similarly, for events with ray path back-azimuths within 27° of the plate motion direction, we used the transverse horizontal component (Table 1). One *S* phase did not have a backazimuth close to the SEPR or plate motion direction (Guatemala), but the results are not sensitive to this event, as discussed in more detail in section 5.4. Since OBSs are deployed at the ocean surface and free fall to the bottom, their resting orientations are not initially known. The azimuth of the horizontal components for each station were established by inference from Rayleigh wave particle motion and P wave first motions [*Hammond*, 2000].

[12] Relative delay times were measured with respect to the IASP91 one-dimensional seismic Earth model [*Kennet and Engdahl*, 1991]. They were determined using cross correlation of up to three cycles of the waveform [*VanDecar and Crosson*, 1990]. Uncertainties in the delay times were estimated by using the method of *VanDecar and Crosson* [1990, equation (8)]. These uncertainties were judged to be implausibly small so an uncorrelated minimum uncertainty was subjectively assigned to be 0.1 s. One standard deviation (1σ) uncertainty values are typically 0.10–0.15 s for *P* waves, and 0.10–0.24 s for *S* waves.

Table 1. Event Locations and Observed Phases[a]

Location	Latitude	Longitude	Date	Time, UT	Phase	Channel	Incidence Angle
Tonga	−15.10	−173.50	13 Nov. 1995	0738:46	*P*	V, DPG	30
New Zealand	−42.99	171.62	24 Nov. 1995	0618:57	*sP*	V, DPG	27
East Pacific Rise	10.16	−104.00	1 Dec. 1995	0520:29	*P, S*	V, DPG	40, 40
Kuril Islands	44.57	149.38	3 Dec. 1995	1801:09	P_{diff}	V, DPG	18
Manzanillo	18.83	−105.48	Dec. 1995	1409:24	*S*	V, DPG	38
Manzanillo	18.58	−105.52	11 Dec. 1995	1944:09	*S*	V, DPG	38
Banda Sea	−6.94	129.18	25 Dec. 1995	0443:24	*SKKSac*	HT	16
Minahassa Peninsula	0.72	119.98	1 Jan. 1996	0805:12	S_{diff}	HT	20
South Kermadec	−32.89	−178.34	30 Jan. 1996	2200:12	*P*	V, DPG	30
Kuril Islands	45.32	149.91	7 Feb. 1996	2136:45	P_{diff}	V, DPG	18
Irian Jaya	−0.95	137.03	17 Feb. 1996	0559:30	$P_{\text{diff}}, S_{\text{diff}}$	V, DPG, HT	18,20
North Peru	−9.62	−79.57	21 Feb. 1996	1251:04	*P*	V, DPG	39
Oaxaca	16.20	−97.96	25 Feb. 1996	0308:19	*P, S*	V, DPG	38, 38
Guatemala	13.02	−91.05	25 Feb. 1996	1417:21	*S*	V, DPG	38
Vanuatu Island	−14.71	167.30	17 March 1996	1448:57	*P*	V, DPG	24
Rat Island	51.22	178.70	22 March 1996	0324:20	*P*	V, DPG	20
Near Nicaragua	11.75	−87.98	27 March 1996	2052:07	*P*	V, DPG	37
Aleutian Island	52.38	−168.68	30 March 1996	1305:18	*P*	V, DPG	21
Tonga	−24.07	−177.08	16 April 1996	0030:54	*P*	V, DPG	30
North Chile	−23.74	−69.96	19 April 1996	0019:32	*sP*	V, DPG	37
Solomon Island	−6.52	155.04	29 April 1996	1440:41	*P*	V, DPG	20
Solomon Island	−4.57	154.83	2 May 1996	1334:29	*P*	V, DPG	19

[a]Latitude, longitude, and incidence angle in the uppermost mantle are in degrees. Phase identifies the part of the teleseismic time series used to measure relative delay times. Channel specifies which of the four recorded components were used, vertical (V), horizontal transverse (HT), or differential pressure gauge (DPG).
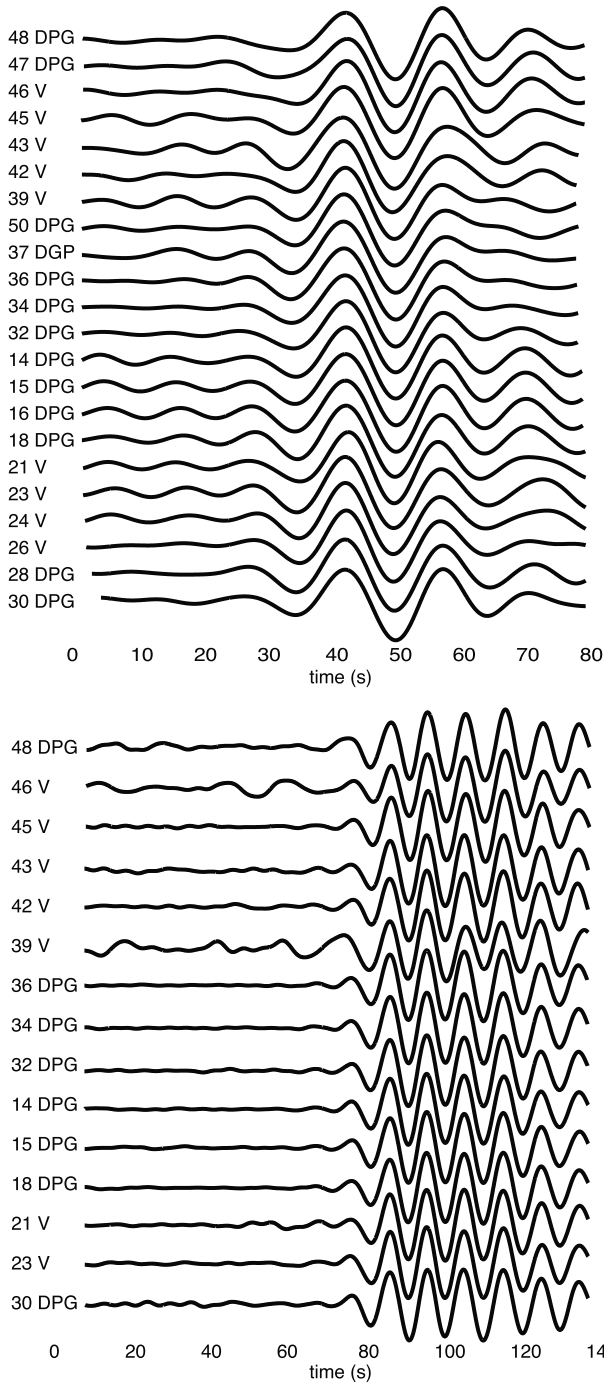
Figure 3. Example waveform data from vertical component (V) seismometers and differential pressure gauges (DPG). The teleseismic (a) S wave arrivals from Oaxaca (25 February 1996) and (b) P wave arrivals from Tonga (16 April 1996) have been amplitude normalized and aligned according to the result of cross correlation. Number preceding channel is the MELT Experiment instrument number.

[13]   The mean delay time for each station (Figure 4) have patterns characterized by wide central zones of positive delays indicating a broad region with anomalously low seismic velocity. The magnitude of these signals is 0.6 s

for P waves, and 3.4 s for S waves. Asymmetry is present, with greater delays on the western flank. Within 75 km of the rise, the P wave signal has a pronounced dip in its pattern, not seen in the S waves. Crustal thickness variations or changes in crustal structure contribute negligibly to these signals, because a change in crustal thickness of one km imparts a P delay of at most 0.04 s. Moreover, crustal thickness measured by *Canales et al.* [1998] is not resolvably different on the east and west side of the SEPR, implying that the crustal contribution to the asymmetry of measured P and S delays is not significant. We attribute the delays to mantle velocity heterogeneity.

4.   Tomographic Method

[14]   We present a tomographic method that allows inversion of body wave delay times for isotropic and anisotropic model parameters. Since the problem is underdetermined, we employ a hypothesis testing approach that introduces a starting model a priori [*Jackson*, 1979; *Tarantola and Valette*, 1982]. For a given starting model, the method determines the perturbations that minimizes a weighted sum of data and model norms.

4.1.   Forward Problem

[15]   To solve the forward problem, we calculate teleseismic delay times **d** from a perturbational slowness model $\Delta\mathbf{u}$ according to

$$\mathbf{d} = \int_{\text{Ray}} \Delta\mathbf{u}\,ds, \qquad (1)$$

where $\Delta\mathbf{u}$ is a function of space and wave propagation direction, and the integral is evaluated along a ray path. The ray geometry is a function of the seismic slowness model **u** which is taken to be the radial reference Earth model IASP91 [*Kennet and Engdahl*, 1991]. Ray paths are calculated with the shortest-path algorithm of *Dijkstra* [1959] and *Moser* [1991], which also determines the travel time and ray path from each station to every point inside the model space. Further details of the graph-theory-based ray tracing are provided by *Toomey et al.* [1994].

[16]   We explicitly assume that the upper mantle is seismically anisotropic. The anisotropy is parameterized with a form that closely approximates velocity dependence in a hexagonally symmetric medium. The seismic velocity is expressed as a function of the angle α between the wave propagation direction and the local anisotropic symmetry axis. For P waves,

$$V_P = V_{P0}\left[1 + \frac{a_P}{2}\cos(2\alpha)\right]. \qquad (2)$$

V_{P0} is the directionally averaged (i.e., isotropic) velocity. This parameterization results from a first-order Taylor expansion of the exact form [*Backus*, 1965], and is accurate for small anisotropy. The magnitude of anisotropy is defined as

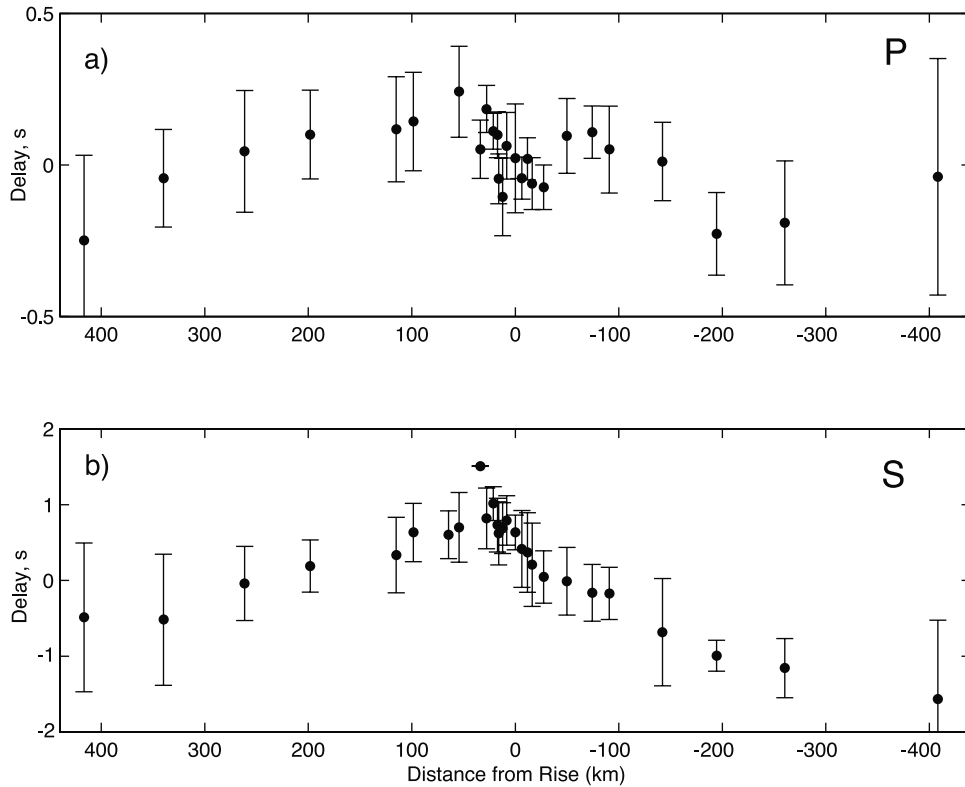$$a_P \equiv 2\frac{\max(V_P) - \min(V_P)}{\max(V_P) + \min(V_P)}, \qquad (3)$$

Figure 4.   Mean (a) P and (b) S wave delays for each station. Vertical bars indicate variation of the delay time observed at the station (not the uncertainties in an observation), plotted at 2 standard deviations.

where max(V_P) (min(V_P)) is the P wave propagation velocity in the fastest (slowest) direction. The relations for V_S are analogous. Shear waves in hexagonally symmetric media do not, in general, exhibit a cos(2α) dependence. However, V_S for the slowest S polarization in the present two-dimensional case does have cos(2α) dependence (Appendix A).

4.2.   Inverse Problem

[17]   We solve the nonlinear tomographic inverse problem

$$\mathbf{G}\Delta\mathbf{m} = \mathbf{d} \qquad (4)$$

for changes to the starting model $\Delta\mathbf{m}$, where $\mathbf{d}$ is an $n \times 1$ vector of delay time data, $\Delta\mathbf{m}$ is the $m \times 1$ vector of perturbations to model parameters, and $\mathbf{G}$ is the Frechet matrix of partial derivatives $\partial t_i/\partial m_j$. The model parameters are divided into four categories: (1) the isotropic P slowness perturbations $\Delta\mathbf{u_P}$; (2) the isotropic S slowness perturbations $\Delta\mathbf{u_S}$; (3) perturbations in the magnitude of anisotropy $\Delta\mathbf{a_P}$; and (4) hypocentral adjustments $\Delta\mathbf{e}$ for each teleseismic event.

[18]   The problem is nonlinear because the partial derivatives in $\mathbf{G}$ are themselves functions of the model parameters $\Delta\mathbf{m}$. This requires recalculating the partial derivatives and recomputing the forward problem for each iteration until convergence is achieved. We assume that velocity heterogeneity in the upper mantle is smooth and of small amplitude, so that the effects of velocity perturbation on ray bending are small. Thus we have kept the ray geometry fixed during successive iterations to save on computational expense. As a result we need calculate the ray paths only

once through the one-dimensional velocity structure. The nonlinearity remains, however, because we solve for a_P, whose Frechet derivatives are functions of a_P. Solving equation (4) iteratively, at the kth iteration

$$\mathbf{G}_k^{-1}\mathbf{d}_k \rightarrow \Delta\mathbf{m_k}, \qquad (5)$$

$$\mathbf{m}_k + \Delta\mathbf{m_k} \rightarrow \mathbf{m_{k+1}}, \qquad (6)$$

$$\mathbf{d}_k - \mathbf{G}_k\Delta\mathbf{m_k} \rightarrow \mathbf{d_{k+1}}, \qquad (7)$$

where $\mathbf{G}_k^{-1}$ is the inverse function performed with the LSQR method [*Paige and Saunders*, 1982]. Iterations continue until changes in the data misfit and m_k are insignificant. More detail is given by *Toomey et al.* [1994].

4.2.1.   The Frechet Derivatives

[19]   The partial derivatives $\partial t_i/\partial m_j$ for the isotropic slowness parameters are the length of the ray segment for which the slowness is valid, scaled by the data uncertainty [*Toomey et al.*, 1994]. For the anisotropic magnitude parameter the derivative of travel time along a ray path with respect to a_P, from equation (2), is

$$\frac{\partial t}{\partial a_P} \approx \frac{\partial u_P}{\partial a_P}\Delta s = \frac{-2u_{P0}\cos(2\alpha)}{[2 + a_P\cos(2\alpha)]^2}\Delta s, \qquad (8)$$

where Δs is the length of the ray path interval over which the velocity at the node is valid, u_{P0} (u_{S0}) is the P (S) wave isotropic slowness, and t is the travel time along the ray path. The relationship is exact when $u_P(u_S)$ is constant over the ray path interval. Since a change in the elastic tensor

Table 2. Elements of the Hexagonal Elastic Tensor[a]

$C_{ij,0}$	$j = 1$	$j = 2$	$j = 3$	$j = 4$	$j = 5$	$j = 6$
$i = 1$	229.10	77.86	77.86	0	0	0
$i = 2$	77.86	205.62	77.86	0	0	0
$i = 3$	77.86	77.86	205.62	0	0	0
$i = 4$	0	0	0	63.86	0	0
$i = 5$	0	0	0	0	68.60	0
$i = 6$	0	0	0	0	0	68.60

[a]Values are in GPa. Abbreviated matrix notation is used so that $C_{11} = c_{1111}$, $C_{22} = c_{2222}$, $C_{33} = c_{3333}$, $C_{44} = c_{2323}$, $C_{55} = c_{1313}$, $C_{66} = c_{1212}$, and $C_{ij} = c_{iijj}$ for $i \neq j$ and $i \leq 3$ and $j \leq 3$.

effects both P and S velocities, a_P and a_S are coupled. We use the tensor described in Appendix A and Table 2 to relate P and S anisotropic magnitudes. The ratio of P to S anisotropy magnitude calculated from this tensor is

$$\gamma_{PS} \equiv \frac{a_P}{a_S} = 1.5. \qquad (9)$$

Thus, for S waves the partial derivative is

$$\frac{\partial t}{\partial a_S} = \frac{-2u_{S0}\cos(2\alpha)}{\left[2 + \frac{a_P}{\gamma_{PS}}\cos(2\alpha)\right]^2}\Delta s. \qquad (10)$$

[20] We restrict the solutions for a_P and a_S to those that can be the result of progressive simple shear deformation of olivine, thus we further require that a_P be positive. To enforce this condition we transform a_P to a logarithmic scale

$$y = \frac{\ln(1000a_P)}{\ln(1000a_{P,\text{pre}})}, \qquad (11)$$

where $a_{P,pre}$ is the anisotropic magnitude in the previous iteration. The partial derivative of travel time with respect to y is

$$\frac{\partial t}{\partial y} = \frac{\partial u_P}{\partial a_P}a_P\ln(1000a_{P,\text{pre}})\Delta s. \qquad (12)$$

Given a perturbation in y, the change in anisotropy will be

$$\Delta a_P = a_{P,\text{pre}}\left[(1000a_P)^{\Delta y} - 1\right]. \qquad (13)$$

[21] Before solving for mantle seismic velocity structure the delay time data are inverted solely for event parameters. Event parameters compensate for errors in hypocentral locations as well as anomalous structure located outside of our study area. Ray parameters $dt/d\Delta$ are calculated from the IASP91 Earth model [Kennet and Engdahl, 1991]. Since there is some trade-off between later origin time and smaller epicentral distance Δ, these parameters are damped so that the magnitude of the greatest change in Δ does not exceed 1°. Changes in event parameters typically reduce the RMS misfit of the data by 10–15%.

4.2.2. Inversion Regularization

[22] Since our problem is underdetermined, we apply conditions of minimum model norm, spatial smoothing,

and a constraint on the relative P and S velocity perturbations in order to stabilize the inversion. Augmenting equation (4) with these constraints provides

$$\begin{bmatrix} \mathbf{F} \\ \lambda_S\mathbf{C}_S \\ \lambda_D\mathbf{C}_D \\ \lambda_{PS}\mathbf{C}_{PS} \end{bmatrix}\begin{bmatrix} \Delta\mathbf{u}_\mathbf{P} \\ \Delta\mathbf{u}_\mathbf{S} \\ \Delta\mathbf{a}_\mathbf{P} \\ \Delta\mathbf{e} \end{bmatrix} = \begin{bmatrix} \mathbf{d} \\ 0 \\ 0 \\ 0 \end{bmatrix}, \qquad (14)$$

where $\mathbf{F}$ now contains the Frechet derivatives, discussed above. Our solution to equation (14) incorporates normalization by the uncertainties in the data [Wiggins, 1972], and an a priori evaluation of model parameter variance. It is equivalent to minimization of the functional

$$s^2 = (\mathbf{d} - \mathbf{G}\Delta\mathbf{m})^T\mathbf{C}_d^{-1}(\mathbf{d} - \mathbf{G}\Delta\mathbf{m}) + \lambda_S\Delta\mathbf{m}^T\mathbf{C}_S{}^T\mathbf{C}_S\Delta\mathbf{m}$$

$$+ \lambda_D\Delta\mathbf{m}^T\mathbf{C}_D{}^T\mathbf{C}_D\Delta\mathbf{m} + \lambda_{PS}\Delta\mathbf{m}^T\mathbf{C}_{PS}{}^T\mathbf{C}_{PS}\Delta\mathbf{m}. \qquad (15)$$

The matrix of smoothing constraints $\mathbf{C}_S$ averages perturbations with those at the adjacent nodes. The relative importance of this constraint is specified by the penalty parameter λ_S, allowing control over the trade-off between model variance and model resolution. Minimization of the model norm is achieved through a damping constraint where $\mathbf{C}_D$ is the diagonal matrix whose elements are one over the product of the starting slowness times the prior uncertainty in the model parameters. This term imposes uniform damping on the percent change in model parameters, weighted by their uncertainty. The relative importance of this constraint is specified by the penalty parameter λ_D. The data covariance $\mathbf{C}_d$ is a diagonal matrix of variances estimated for the body wave delay times. The matrix $\mathbf{C}_{PS}$ describes the constraint between P and S slowness perturbations.

[23] A constraint between the perturbation in P and S slownesses enforces the knowledge that these quantities are not independent. We try three forms of V_P to V_S coupling: (1) V_P/V_S is assumed to be unchanged from that of the starting model, (2) the variations in V_P/V_S are assumed to be spatially smooth, and (3) the value $\partial\ln V_S/\partial\ln V_P$ is constant throughout the model. The advantage of using constant V_P/V_S is that the constraint is relatively strong so fewer effective model parameters are active. Constraining V_P/V_S smoothness has the advantage of being independent of any assumed starting V_P/V_S or $\partial\ln V_S/\partial\ln V_P$ value. We implement this constraint by noting that

$$\delta\left(\frac{V_P}{V_S}\right) = \frac{V_S\delta V_P - V_P\delta V_S}{V_S{}^2} \qquad (16)$$

and spatially average this function

$$\delta\left(\frac{V_P}{V_S}\right)_i = \sum_{j \neq i} w_j\delta\left(\frac{V_P}{V_S}\right)_j \qquad (17)$$
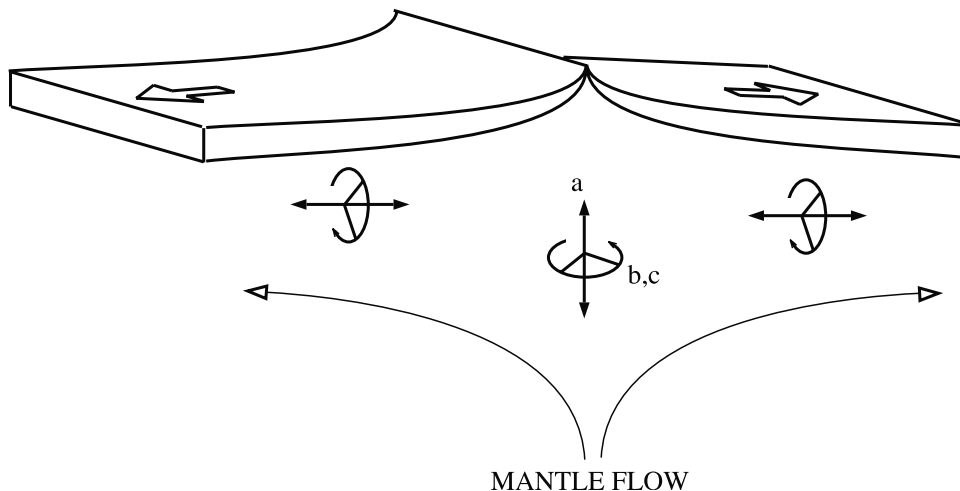
Figure 5. Prior expectation for anisotropy beneath the southern East Pacific Rise. Schematic mantle upwelling is characterized by a horizontal flow beneath the flanks, and vertical upwelling beneath the ridge (curved arrows). The resulting shear deformation preferentially aligns olivine *a* axes, and hence the *P* wave fast propagation direction, vertically beneath the ridge and horizontally on the flanks (straight arrows with rings). The anisotropy is simplified by assuming that the olivine *b* and *c* axes are randomly distributed around the *a* axis. Adapted from *Nishimura and Forsyth* [1989] with permission from Blackwell Publishing.

with the Gaussian weights w_j described by *Toomey et al.* [1994]. To fix $\partial \ln V_S / \partial \ln V_P$, we approximate and convert to slowness,

$$\frac{\partial \ln V_S}{\partial \ln V_P} \approx \frac{V_P}{V_S} \frac{\Delta V_S}{\Delta V_P} \tag{18}$$

$$\approx \frac{V_S}{V_P} \frac{\Delta u_S}{\Delta u_P}. \tag{19}$$

5. Analysis

[24] In applying our tomographic technique to the MELT data we make several simplifying assumptions. First, owing to the array geometry and the presumption that structures along this section of the mid-ocean ridge are largely two-dimensional, we restrict our inversions to determining variations in a vertical plane normal to the ridge axis. Second, we simultaneously invert the *P* and *S* delay time data against a range of anisotropic starting models. This hypothesis-testing approach has several advantages, for example: we can test simple anisotropic structures that have geodynamic relevance; we can find simple models of anisotropy that adequately fit the shear wave splitting data; and the number of additional free parameters introduced to the inverse problem is kept relatively small. The anisotropic starting models are systematically varied in a grid search in order to determine the sensitivity of the delay time data to seismic anisotropy. We show that the delay time data are indeed sensitive to the orientation, magnitude, and distribution of anisotropy beneath the SEPR. For each tomographic solution we compute the predicted shear wave splitting and compare to the measurements of *Wolfe and Solomon* [1998]. On the basis of the misfits to the delay time and shear wave splitting data we exclude certain classes of anisotropic

starting models and, by inference, certain models of mantle flow.

5.1. Seismic Anisotropy and Mantle Flow

[25] Our choice of the form and distribution of seismic anisotropy has been guided by previous seismic investigations of the Pacific upper mantle, by theoretical and laboratory studies of mantle rheology and flow, and by geologic observations of exhumed mantle rocks. Because of these considerations we make the approximation that upper mantle rocks are hexagonally anisotropic (Appendix A). The approximation may not be universally valid, however, it is surely an improvement over the usual assumption that the upper mantle is isotropic. Furthermore, we simplify the parameterization of the anisotropic model by assuming that it is constant inside each of a few domains.

[26] Regional and global seismic studies are consistent with azimuthal *P* wave anisotropy in oceanic basins away from ridges (Figure 5). Such studies have used surface wave dispersion [*Forsyth*, 1975; *Montagner and Nataf*, 1986; *Nishimura and Forsyth*, 1989], body wave travel times [*Dziewonski and Anderson*, 1981; *Ekström and Dziewonski*, 1998] and shear wave splitting [*Wolfe and Solomon*, 1998; *Wolfe and Silver*, 1998] to characterize the anisotropy in the Pacific upper mantle. For azimuthal anisotropy in off-axis mantle, the fast direction is oriented roughly parallel to modern plate motion, [e.g., *Hess*, 1964; *Raitt et al.*, 1969; *Montagner and Nataf*, 1986; *Nishimura and Forsyth*, 1989]. In the off-axis regions of the MELT area, surface waves have been used by *Forsyth et al.* [1998] to infer that the seismic fast axis is subnormal to the SEPR, a result consistent with shear wave splitting measurements [*Wolfe and Solomon*, 1998]. In the vicinity of a spreading center, seismic studies that sample only the shallowmost upper mantle using *Pn* data also report the presence of azimuthal anisotropy [*Dunn and Toomey*, 1997]. Seismic methods which sample to deeper depths, however, are generally

consistent with lesser amounts of azimuthal anisotropy (Figure 5) [*Nishimura and Forsyth*, 1989; *Ekström and Dziewonski*, 1998].

[27] A more detailed prediction of the pattern of seismic anisotropy beneath a mid-ocean ridge is provided by a combination of observations of deformed upper mantle rocks [*Peselnick and Nicolas*, 1978; *Christensen*, 1984; *Nicolas and Christensen*, 1987; *Kern*, 1993; *Mainprice*, 1997], laboratory studies of rock deformation [*Zhang and Karato*, 1995] and the theory of plastic deformation of polycrystalline materials [*Ribe*, 1989; *Wenk et al.*, 1991; *Ribe*, 1992; *Kaminski and Ribe*, 2001]. These studies indicate that progressive simple shear results in the crystallographic alignment of olivine, such that the *a* axis of olivine [100] (seismically fastest) rotates into the foliation plane and parallel to the direction of transport. The *b* axis of olivine [010] (seismically slowest) aligns normal to the foliation plane. The resulting aggregate has orthorhombic elastic symmetry, with the fastest *P* wave propagation direction lying in the foliation plane, parallel to the direction of transport. To simplify our modeling we choose to limit the detail in the anisotropy inferred from the MELT data to the hexagonal symmetry most closely approximating the orthorhombic symmetry, because it is the simplest extension from isotropic capable of explaining the seismic observations. For a fast spreading ridge, progressive simple shear is likely in two places: beneath the flanks of the rise as the lithosphere moves over a more stationary mantle interior, and beneath the spreading axis where mantle flow velocity gradients in the upwelling zone provide vertically oriented progressive shear strain. In the presence of simple shear, the dominant orientation of the olivine [100] axis is predicted to be in the transport direction, i.e., subvertical in the upwelling zone beneath the ridge and subhorizontal beneath the flanks. These predictions are supported by numerical models of two-dimensional subaxial flow and the response of olivine aggregates to the associated finite strains [*Blackman et al.*, 1996; *Blackman and Kendall*, 1997; *Tommasi et al.*, 1998].

5.2. Grid Search for Anisotropy

[28] We test the data against a variety of starting models having simple distributions of anisotropy. Each starting model contains three quadrilateral domains of homogeneous anisotropy. These have purposefully been made as simple as possible in order to minimize the number of additional parameters in the tomographic inversion. Two of the domains lie beneath the eastern and western flanks of the ridge and have fixed horizontal, hexagonal symmetry axes (Figure 6). The thickness of the anisotropic layer is 200 km. This thickness is not well constrained by the shear wave splitting measurements, but it is likely greater than 100 km, since a thinner layer would require magnitudes of S wave polarization anisotropy greater than those observed in samples of upper mantle material (3–6%) [*Mainprice and Silver*, 1993], and greater than those consistent with azimuthal anisotropy of Rayleigh wave propagation [*Forsyth et al.*, 1998]. Our tomographic images are not particularly sensitive to the thickness of this layer, provided that it is between 100 and 300 km thick. The magnitude of anisotropy a_P is held fixed in the flanks, and made consistent with the average shear wave split time for each flank, as
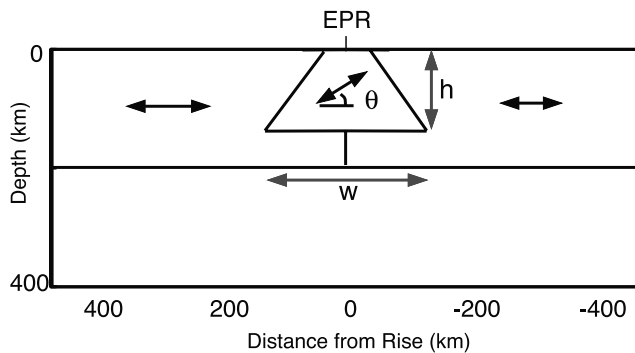

Figure 6. Geometry of the anisotropy domains used in the starting model. Anisotropy is homogeneous inside each of the three domains. The 200 km thick flanks have horizontal anisotropic fast propagation direction parallel to plate motion with magnitude consistent with the shear wave splitting observations of *Wolfe and Solomon* [1998] (see text). The central, subridge domain has width w at the bottom, depth h, and dip θ of fastest V_P direction. The model is isotropic below 200 km.

measured by *Wolfe and Solomon* [1998]. The western flank is assigned $a_P = 5.6\%$ and the eastern flank $a_P = 3.2\%$. In the central region beneath the ridge the dip of anisotropy θ is varied, as is the size of this region. The central domain is trapezoid shaped, and 40 km wide at the top with width at the bottom $w = 80$, 160 or 320 km and depth $h = 80$, 180, or 280 km (Figure 6). The dip θ is either 0°, 30°, 60°, 90°, −30°, or −60°, with negative values indicating a westward dip. The dimensions of the eastern and western domains are adjusted so that they fit flush against the central subridge domain.

[29] For each size of the central domain and each anisotropy orientation we solve the tomography problem, obtaining P and S velocity models. Since the orientations of anisotropy are fixed within each domain and the magnitude is fixed within the eastern and western flanks, the number of model parameters for seismic anisotropy is reduced to one, the magnitude of anisotropy within the central domain. The associated misfit of the body wave delay time data is measured as

$$\chi_{tt}^2 = \frac{1}{n_1}(\mathbf{d} - \mathbf{G}\Delta\mathbf{m})^T \mathbf{C}_d^{-1}(\mathbf{d} - \mathbf{G}\Delta\mathbf{m}), \qquad (20)$$

where n_1 is the number of delay time data.

5.3. Shear Wave Splitting

[30] Compatibility of the models obtained in the grid search with the shear wave splitting observed by *Wolfe and Solomon* [1998] is an additional measure of model quality. To calculate the predicted split times, we consider vertically propagating S waves (e.g., *SKS*) with polarizations parallel and normal to the ridge. These directions are good approximations to the observed polarizations and they are consistent with hexagonal anisotropy when the symmetry axis lies in the vertical plane normal to the ridge.

[31] The elastic moduli for splitting calculations are determined by scaling the abbreviated form elastic tensor $C_{ij,0}$ (Appendix A and Table 2) to match V_S and a_P at each

node along the vertical ray path. $C_{ij,0}$ is derived from laboratory measurements of Ivrea zone peridotite [*Kern*, 1993], and serves as the model form of anisotropy. We preserve the symmetry and scaling of P to S anisotropies γ_{PS} of $C_{ij,0}$ by defining the adjusted tensor $C_{ij,anis}$ with arbitrary magnitude of anisotropy a_P as

$$C_{ij,\text{anis}} = A\left(C_{ij,0} - C_{ij,\text{iso}}\right) + C_{ij,\text{iso}} \qquad (21)$$

where $C_{44,\text{iso}} = C_{55,\text{iso}} = C_{66,\text{iso}} = \frac{1}{3}\sum_{i=4}^{6} C_{ii,0} = \mu_{\text{iso}}$ is the directionally averaged shear wave modulus of $C_{ij,0}$, and A scales the anisotropy to match a_P. The other components of $C_{ij,\text{anis}}$ do not matter because we are here only concerned with shear waves in hexagonally symmetric media. Matching respectively the maximum (μ_{max} and $\mu_{\text{max},0}$) and minimum (μ_{min} and $\mu_{\text{min},0}$) shear components of $C_{ij,\text{anis}}$ and $C_{ij,0}$ leads to

$$\mu_{\text{max}} = A\left(\mu_{\text{max},0} - \mu_{\text{iso}}\right) + \mu_{\text{iso}} \qquad (22)$$

$$\mu_{\text{min}} = A\left(\mu_{\text{min},0} - \mu_{\text{iso}}\right) + \mu_{\text{iso}}. \qquad (23)$$

Combining the definitions (3) and (9) and relation $V_S = \sqrt{\mu/\rho}$ allows elimination of μ_{min} with

$$\mu_{\text{min}} = \mu_{\text{max}}\left(\frac{2\gamma_{PS} - a_P}{2\gamma_{PS} + a_P}\right)^2. \qquad (24)$$

Solving equations (22) and (23) for A, we obtain

$$A = \frac{\mu_{\text{iso}}(B - 1)}{\mu_{\text{min},0} - \mu_{\text{iso}} - B\left(\mu_{\text{max},0} - \mu_{\text{iso}}\right)} \qquad (25)$$

where

$$B = \left(\frac{2\gamma_{PS} - a_P}{2\gamma_{PS} + a_P}\right)^2. \qquad (26)$$

The shear wave splits are calculated from

$$C_{ij} = \frac{V_S^2 \rho}{\mu_{\text{iso}}}, \qquad (27)$$

so that the directionally averaged shear velocity is V_S.

[32] Integrating the anisotropic slownesses along vertical paths provides an estimate of the travel time observed at a MELT receiver. The differences between travel times of shear waves polarized parallel and normal to the rise axis are the predicted split times $d\mathbf{t}_{\text{pred}}$. The velocity of the shear waves are determined from C_{ij} (Appendix A). The misfit between the split measurements and the predicted time is given by

$$\chi_{ss}^2 = \frac{1}{n_2}\left(\delta\mathbf{t} - d\mathbf{t}_{\text{pred}}\right)^T \mathbf{C}_{ss}^{-2}\left(\delta\mathbf{t} - d\mathbf{t}_{\text{pred}}\right), \qquad (28)$$

where $\mathbf{C}_{ss}$ is the diagonal matrix containing the uncertainties in the split measurements from *Wolfe and Solomon* [1998], n_2 is the number of stations, and $\delta\mathbf{t}$ are the measured split

delay times. For each tomographic model the misfits to the observed splits are presented in the Results section.

5.4. *S* Wave Data Selection

[33] In the presence of anisotropy, the determination of S wave delay times requires isolation of a particular shear polarization. Failure to do so will result in waveform distortion [*Silver and Chan*, 1991] that may vary between sites, giving rise to errors in delay time measurements. We chose to measure delay times from the slower S wave polarization because its $\cos(2\alpha)$ directional velocity dependence is similar to that of the P wave (Appendix A), simplifying the parameterization of anisotropy. Within the MELT area the slow polarization is uniformly parallel to the ridge [*Wolfe and Solomon*, 1998] (Figure 1).

[34] Because we vary the dip of the anisotropic symmetry axis beneath the rise, not all S slow phases are predicted to be polarized parallel to the rise. Thus, to be consistent with each of the dips used in the tomographic grid search, we must consider excluding delays measured from S arrivals at near-axis stations. As a test, we predict the azimuth of the slow and fast polarizations for each S wave in the MELT data by projecting to the surface the eigenvectors of the Christoffel matrix having the two lowest eigenvalues (Appendix A). We identify S waves that have significant shear wave splitting and slow polarizations with azimuths greater than $15°$ from normal to the rise axis. We then perform the tomographic grid search with and without this set of S wave delay times, and find that the results are similar in both cases, with respect to both the velocity heterogeneity and the preferred dip of anisotropy. It is not surprising that the anisotropy is largely constrained by the P waves, since V_P has a greater sensitivity to the direction of wave propagation. Since constraint on the S wave velocity heterogeneity is improved by including all delay times, we have included these S wave delays in the final results.

5.5. Synthetic Tests

[35] Inversions of synthetic data are used to test the ability of the data to resolve anomalous structure. For a known seismic model we calculate synthetic delay times using the actual MELT data P and S ray sets (Figure 7). To simulate the presence of delay time noise we add random Gaussian uncertainties ($\sigma_P = 0.12$ and $\sigma_S = 0.17$) to the synthetic data. The first synthetic model is a checkerboard structure that assesses the ability of the MELT data to resolve features that vary with depth and distance from the rise. Figure 8 shows the results of several inversions for different coupling between V_P and V_S and different squeezing depths, Z_S. Z_S is the depth of bottom of the model, below which we do not solve for structure. The results suggest that resolution is good within 200 km of the rise. The location and size of the reconstructed blocks is also close to that of the starting model. For deeper regions beneath the flanks, especially >200 km east of the ridge and >300 km west of the ridge, there is noticable streaking along ray paths. This is due to the presence of fewer crossing ray paths in these areas. Figures 8c–8f show results of inversions with $Z_S = 400$ and 600 km. In Figures 8e and 8f, the deeper blocks have been stretched down toward the lower boundary, and there is marked irregularity in their shapes. The horizontal boundaries between the
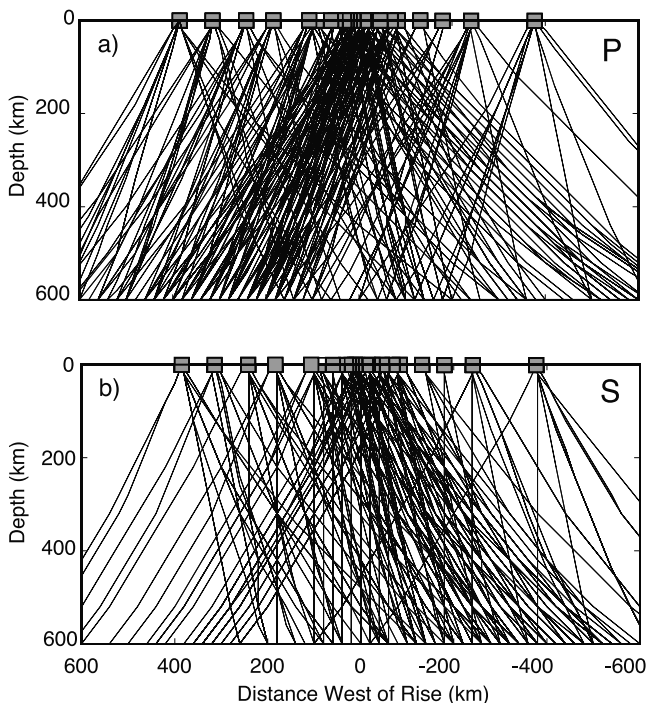
Figure 7. (a) *P* and (b) *S* wave ray paths determined by the shortest path method.

uppermost and middle layers are relatively unchanged, however, indicating that above 300 km depth, the inferred heterogeneity is not a function of the applied squeezing depth. Because of this, and because the results of *Toomey et al.* [1998] show that structure below 400 km is not required to explain the data, we use $Z_S = 400$ km for the remainder of the modeling presented here. In Figures 8g and 8h the constraint between *P* and *S* wave velocity has been changed so that $\partial \ln V_S / \partial \ln V_P = 2.2$ everywhere in the model, the same as in the synthetic structure. The magnitude of the *S* wave anomalies are slightly increased and *P* wave anomalies slightly decreased compared to Figures 8e and 8f, but their shapes are nearly identical. Therefore this stronger constraint provides little improvement, compared to the smooth V_P / V_S constraint, in the ability of the data to reconstruct the shape of anomalous regions of seismic velocity.

[36] To counter an undesirable effect of spatial smoothing, we apply an additional damping to the top row of the model. Our spatial smoothing constraint provides an unnatural tendency for velocity perturbations to gather at the edges of the model. This is especially problematic at the top of the model, where the greater concentration of crossing rays provides more opportunity for the assignment of velocity perturbations. We assign the value of damping on the top row to be 400 times the damping applied to the rest of the model, a value determined through trial and error modeling of the synthetic data. The effect of this damping of the top row can be seen in the reconstructed models in Figure 8. Below, we remove this constraint to evaluate its effect on the model misfit and on the inferred velocity pattern.

[37] Other synthetic tests we have performed with variously shaped and located blocks of anomalous seismic velocity and varying $\partial \ln V_S / \partial \ln V_P$ are not shown here for the sake of brevity. Their results are qualitatively similar to those of the checkerboard test. To summarize these tests: the resolution is best within 200 km of the rise axis, and resolution is worst in the regions deeper than 250 km and farther than 200 km from the rise axis, corresponding to regions of the least beneficial crossing ray geometry. Vertical smearing of up to 100 km was common. Accurate reconstruction of the magnitude of *S* wave velocity perturbations was mostly affected by the type of coupling between *P* and *S* wave velocities. Use of the fixed $\partial \ln V_S / \partial \ln V_P$ constraint provided superior reconstruction of anomaly shape, while smooth changes in V_P / V_S best reproduced the magnitude of the *S* anomaly.

[38] A second class of synthetic test evaluated the ability of the data and our method to recover anomalous isotropic structure in the presence of a domain of anisotropy, and to identify simultaneously the most likely distribution and orientation of anisotropy. These synthetic models (Figures 9a and 9b) contain an anisotropic region 160 km wide at the bottom and 180 km deep, with the hexagonal symmetry axis dipping 60° to the west; the magnitude of anisotropy, a_P, is 6.0%. The V_P and V_S isotropic anomalies span a region 340 km wide and 220 km deep, centered on the rise axis. The peak *S* wave anomaly is −8.8% while the peak *P* wave anomaly is −4.0%. This structure has been smoothed so that velocity perturbation grades from zero to the peak value across a transitional band 80 km wide.

[39] We performed a grid search, as described above, on this synthetic data. The search finds that the model with minimum misfit has an anisotropic domain with the correct dimensions and dip of anisotropy. Figure 9e shows the model misfit as a function of anisotropy dip angle and the dimensions of the central domain. For all central domain sizes, *P* wave fast propagation directions dipping 60° to the west fit the data best. The sensitivity to the dip of anisotropy and to the shape of the anisotropic domain, as measured by the difference between the maximum and minimum χ^2_{tt}, are similar. Inversion of the synthetic data produces a low-velocity anomaly whose shape has been well reconstructed, although about 100 km of vertical smearing of the anomaly is observed and higher-velocity regions emerge beneath the east and west flanks. These high-velocity artifacts arise because of the imposed damping constraint, which requires that a weighted sum of the model perturbations be zero. Very little east-west asymmetry in the isotropic heterogeneity has been introduced, even though the dipping anisotropy causes an east-west asymmetry in the synthetic delay time signals, implying that the method effectively compensates for the presence of simple regions of anisotropy. The peak-to-peak horizontal V_P and V_S amplitude changes are 4.8% and 8.5%, respectively, close to those of the synthetic structure.

6. Results

[40] In this section we present the results of tomographic inversions that use isotropic and anisotropic starting models. For a range of starting models, a comparison of the resulting data misfits shows that structures with seismic anisotropy in a few discrete domains fit the data as well as, and in many cases significantly better than, isotropic models. We dem-
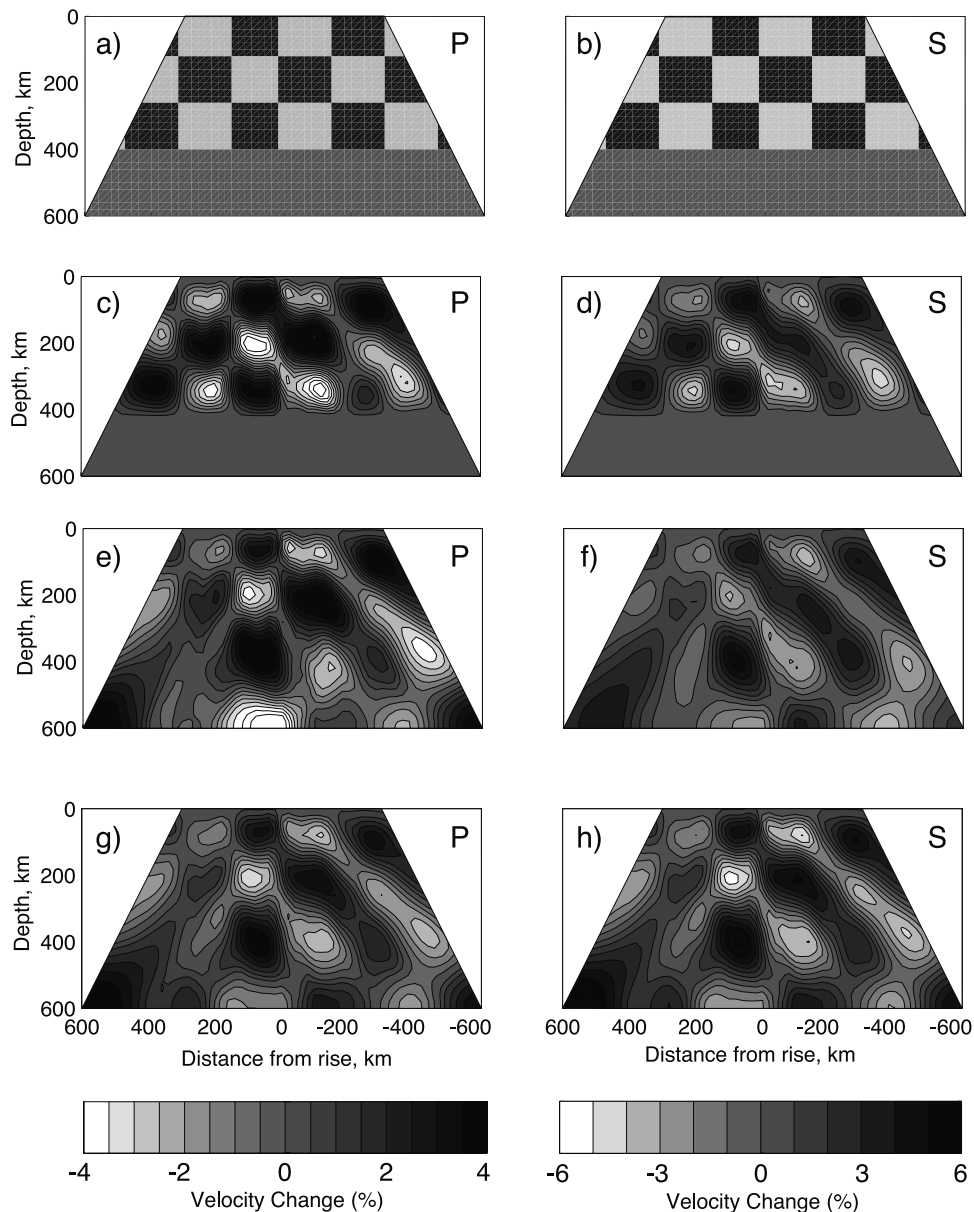
Figure 8.   Synthetic checkerboard models with (a) ±2% V_P and (b) ±4.4% V_S velocity anomalies. Result of inversion of synthetic data (c and d) with squeezing depth $Z_S = 400$ km and smooth V_P/V_S, (e and f) with $Z_S = 600$ and smooth V_P/V_S, and (g and h) with $Z_S = 600$ and fixed $\partial \ln V_S/\partial \ln V_P = 2.2$.

onstrate that the data misfit is sensitive to the orientation of anisotropy, and that the misfit is at a minimum when the an isotropic symmetry axis is near horizontal in the central subridge domain. For all models we compare the predicted shear wave splitting to the observations [*Wolfe and Solomon*, 1998]. A combination of the delay time inversions and the splitting analysis eliminates models containing vertically oriented symmetry axes in any region thicker than 80 km. We also show that this result is insensitive to the form of constraint between V_P and V_S.

6.1.   Isotropic Solutions

[41]   We begin with isotropic inversions (Figure 10) to provide a basis of comparison for the anisotropic solutions. The starting model is the IASP91 one-dimensional Earth model [*Kennet and Engdahl*, 1991]. Horizontal and vertical

Gaussian smoothing with half width $\tau_x = \tau_z = 20$ km [*Toomey et al.*, 1994] and weighting $\lambda_S = 500$ are applied. The a priori variance in model parameters is 2% for P waves and 4% for S waves. Since there are fewer S residuals, they have been given proportionally more weight to allow them equal influence on the result. Damping of $\lambda_D = 40$ is applied everywhere, and the additional damping of the top row is applied to compensate for the effects of smoothing at the top edge of the model. The V_P/V_S smoothing constraint is $\lambda_{PS} = 500$. The inversion results, for three different types of constraint between V_P and V_S, are shown in Figure 10.

6.1.1.   East-West Asymmetry in V_P and V_S

[42]   In each isotropic model, V_P and V_S are asymmetric with respect to the rise, with lower velocities beneath the western flank. In the model with a smooth V_P/V_S constraint (Figures 10a and 10b), the magnitude of the V_P and V_S
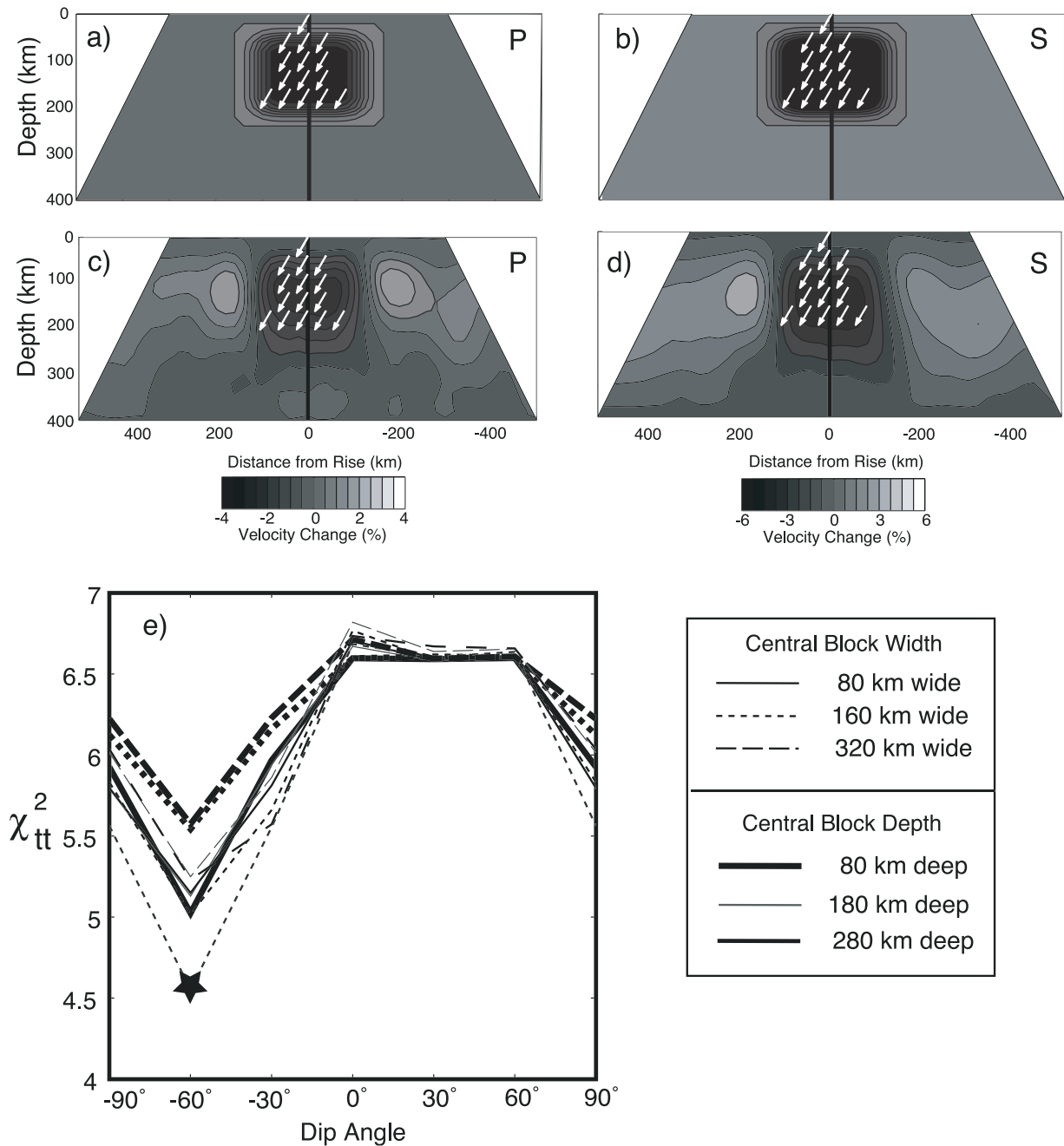
Figure 9. Synthetic (a) V_P and (b) V_S models with isotropic and anisotropic velocity anomalies. A rectangular region of -4% V_P and -8.8% V_S has been smoothed to 340 km wide and 220 km deep. The region of anisotropy is 160 km wide on the bottom, 180 km deep, and has $a_P = 6\%$. Reconstruction of the (c) V_P and (d) V_S anomalies as determined by the grid search method. (e) Relationship between the dip angle of anisotropy and the data misfit χ_{tt}^2. Line type (solid, short dashed, long dashed) denotes the width of the anisotropic subridge domain in the starting model, and line weight (thick black, thin gray, thin black) denotes its depth.

anomalies are about 1.0% and about 2.75%, respectively. The low V_P anomaly region has two lobes, one beneath the rise and extending from about 80 km to more than 200 km deep, and one is ~80–200 km west of the rise extending to over 220 km deep. We note that elongation of the low-velocity anomaly in depth is a feature common to most of our isotropic inversions. The separation of the V_P anomaly into two lobes is also a common characteristic in our

isotropic inversions but not of our anisotropic inversions which may indicate that it is an artifact of anisotropy. The two-lobe structure is not shared by the V_S anomaly.

6.1.2. V_P to V_S Coupling

[43] The form of constraint between V_P and V_S has a significant effect on the inferred S wave heterogeneity. When the V_P/V_S smoothness constraint is used, there is a single pronounced low V_S region that dips westward.
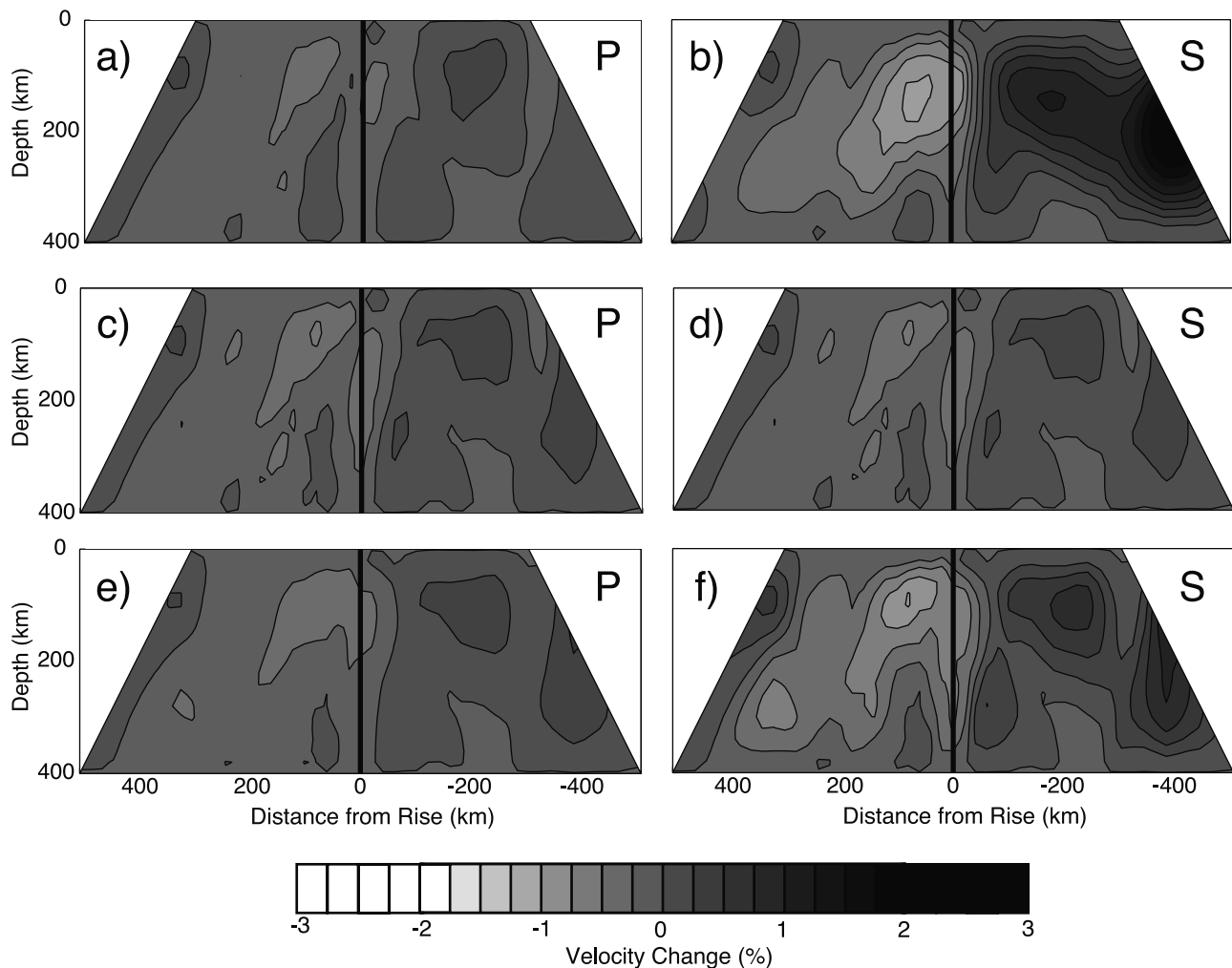
Figure 10. Results of inversions with one-dimensional isotropic starting models. (a) V_P and (b) V_S models with smooth V_P/V_S, (c and d) with fixed $\partial \ln V_S/\partial \ln V_P = 1.0$, and (e and f) with $\partial \ln V_S/\partial \ln V_P = 2.2$.

Introduction of the stronger form of coupling where $\partial \ln V_S/\partial \ln V_P = 1.0$ everywhere (Figures 10c and 10d), causes the V_S anomaly to conform to the V_P anomaly. V_P remains relatively unchanged except that the magnitude of the V_P anomaly has changed by ~0.25%. V_P retains its two lobed structure. When $\partial \ln V_S/\partial \ln V_P = 2.2$ (Figures 10e and 10f) the two lobed V_P structure flattens into a single region, while the V_S anomaly has a magnitude and distribution more similar to V_S subject to the V_P/V_S smooth constraint, although the lowest velocities are more shallow.

6.2. Anisotropic Solutions: Grid Searches

[44] We now consider solutions where the starting model contains anisotropy on the flanks of the rise, consistent with observed shear wave splitting, and a region of dipping anisotropy beneath the rise. Separate grid searches are performed for the same V_P to V_S constraints used in the isotropic inversions. For each trial model, a different starting velocity structure is used that includes anisotropy beneath the rise flanks and a subridge domain whose shape and dip of anisotropy vary (Figure 6). The damping and smoothing parameters are the same as for the

isotropic models. For every model the fit to the delay time and shear wave splitting delays are determined using equations (20) and (28). The results for V_P to V_S constraints of smooth V_P/V_S and $\partial \ln V_S/\partial \ln V_P = 2.2$ are summarized in Figure 11. The results for V_P/V_S fixed are qualitatively similar to those where $\partial \ln V_S/\partial \ln V_P = 2.2$ except that the χ_{tt}^2 values are higher. For each anisotropic central domain we show the misfit to the delay times (Figures 11a and 11b) and to the shear wave splitting observations (Figures 11c and 11d). The threshold above which models fit worse than the best fitting models to 95% confidence is indicated by the gray horizontal bar. These confidence levels are defined by $\chi_{p,n}^2 = F_{p,n}\chi_{min}^2$, where $F_{p,n}$ is the F test critical value for degrees of freedom n, at confidence level p, and χ_{min}^2 is the misfit of the best fitting model. In particular, we find $F_{0.95,462} = 1.16$. The data misfit of the isotropic model with the same V_P to V_S constraint is shown with a dashed horizontal bar. In all, we present the results and summaries of over 300 inversions of the data.

6.2.1. Effect of Anisotropy on Velocity Heterogeneity

[45] The presence of anisotropy controls the distribution of velocity heterogeneity beneath the SEPR in three impor-
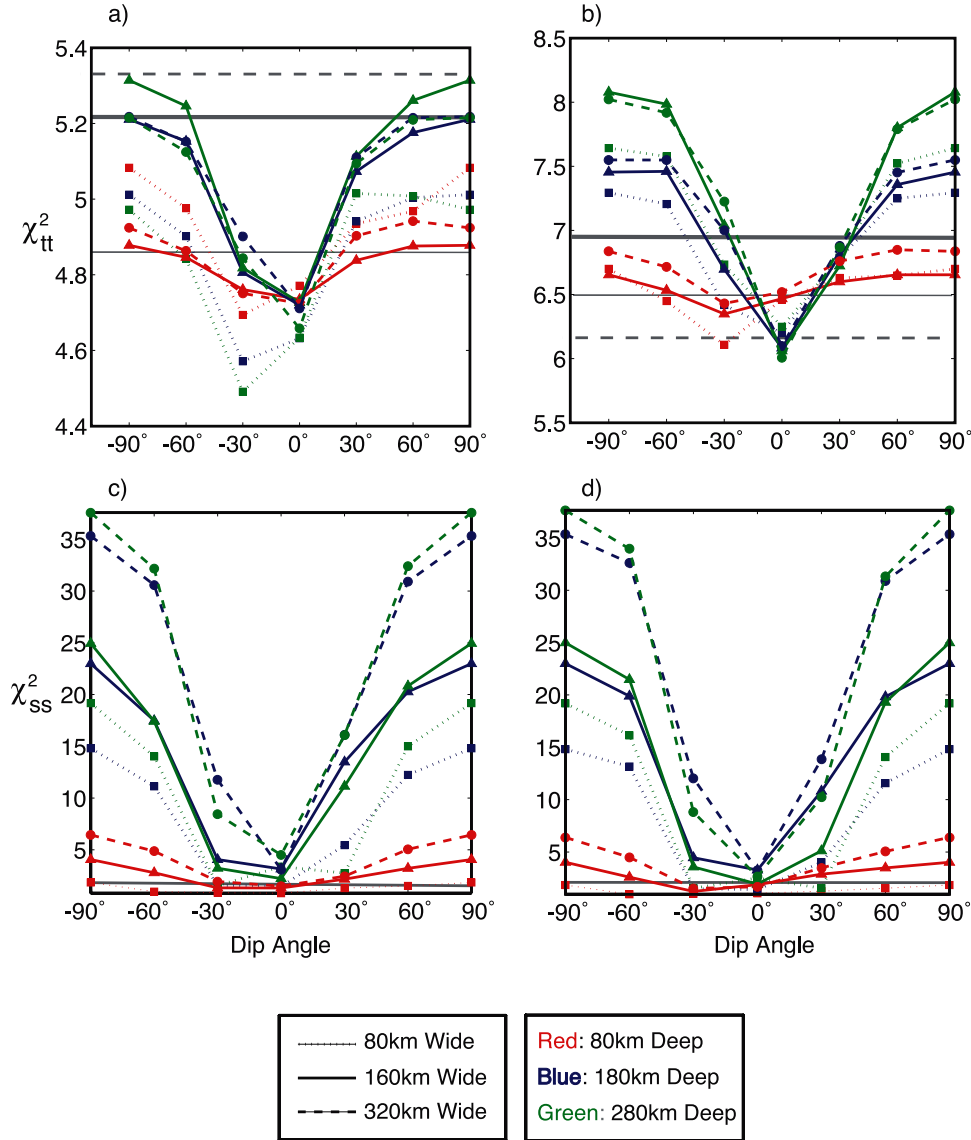
Figure 11. Misfits to (a and b) body wave delay times and (c and d) shear wave splitting delays as a function of dip in anisotropic symmetry axis. The constraint between V_S and V_P is smooth V_P/V_S (Figures 11a and 11c), and $\partial\ln V_S/\partial\ln V_P = 2.2$ (Figures 11b and 11d). Models with misfit significantly greater than the best fitting model, to 95% (80%) confidence, fall above the thicker (thinner) gray horizontal bar. The misfit of the isotropic model with the same V_P to V_S constraint is shown with the dashed horizontal line.

tant ways. Two of the best fitting anisotropic starting models, having $h = 180$ km, $w = 160$ km, $\theta = 0°$, and $h = 80$ km, $w = 80$ km, $\theta = -30°$, are shown in Figure 12. First, in comparison with the isotropic results, the magnitude of the velocity anomalies are greater in the presence of anisotropy. This occurs because of a decrease in the volume of the subridge anomaly and because of the competing effects of isotropic and anisotropic structures. The peak-to-peak V_P and V_S anomalies measured within a horizontal layer at the depth of maximum variation (typically $\sim$100–120 km) are functions of the size and orientation of the subridge domain of anisotropy. However, the peak-to-peak velocity anomalies do not vary greatly among the models that fit the data well. In the best fitting model the greatest peak-to-peak V_P amplitude within a horizontal layer is 1.9%, while the peak-to-peak V_S amplitude is 2.7%. We

have measured the peak-to-peak anomalies within ±300 km of the rise in order to consider only the region where tomographic constraint is best. Second, the degree of asymmetry is a strong function of the anisotropic starting model. A comparison of Figure 12 to Figure 10 shows a large reduction of asymmetry in the lowest isotropic velocities in the upper 200 km when the anisotropic rise flanks are introduced, but in all well-fitting models significant isotropic asymmetry remains. The size, shape and dip of the anisotropic region beneath the rise influences the shape of the near ridge isotropic anomalies. For example, a fast axis dipping 30° west (Figure 12h), requires lower isotropic velocities in the deep western mantle (>200 km depth). The effect of fast axis orientation on the misfit (Figure 11) and on the inferred heterogeneity increases with the size of this domain. Third, the narrow vertical region of low
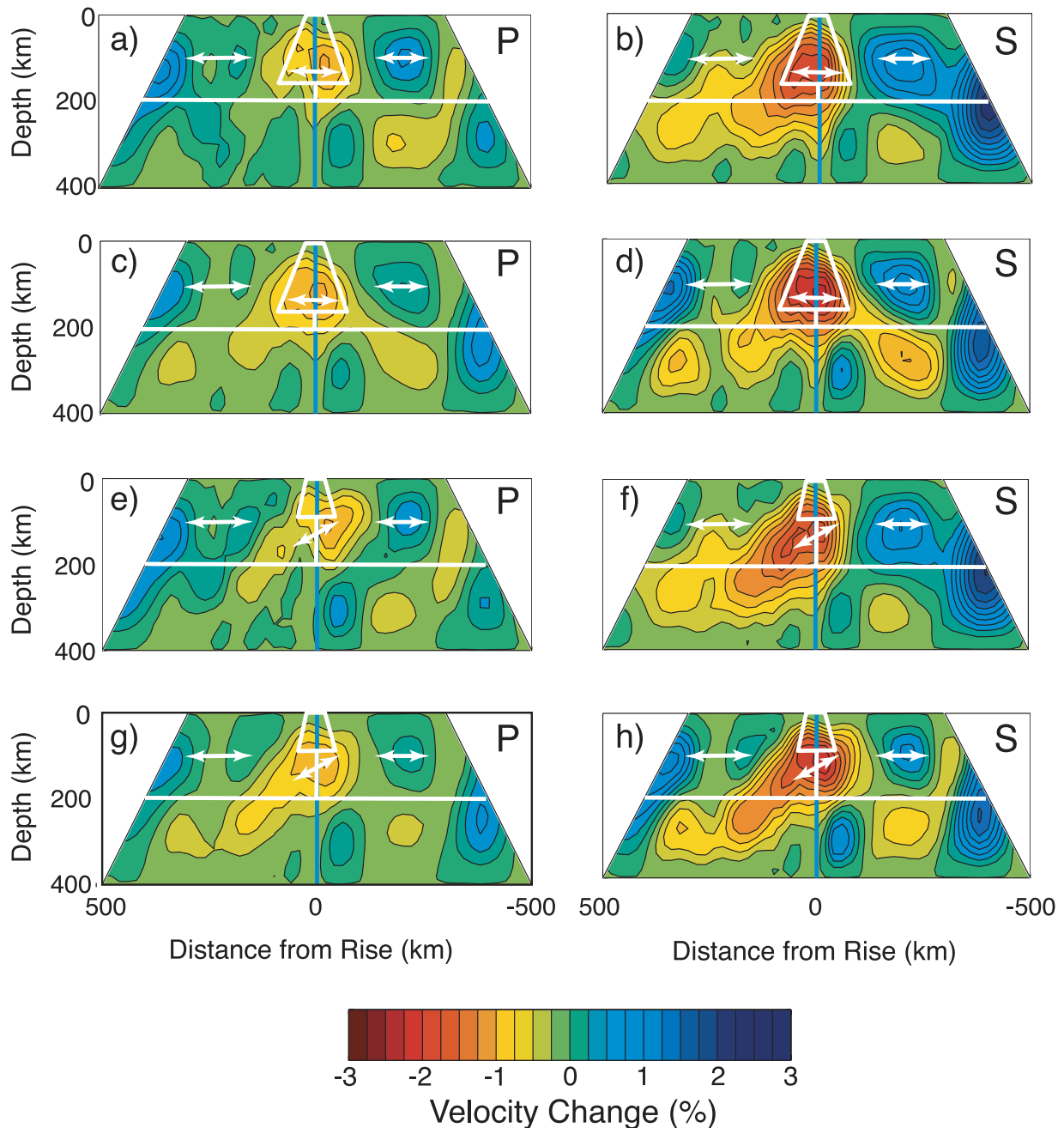
Figure 12. Models among those best fitting the data. Models having starting anisotropic central domain (a and b) with $w = 160$, $h = 180$, $\theta = 0°$ having smooth V_P/V_S and (c and d) with $\partial \ln V_S/\partial \ln V_P = 2.2$. (e, f, g, and h) Same as Figures 12a, 12b, 12c, and 12d, respectively, with a starting model with anisotropic region with $w = 80$, $h = 80$, $\theta = -30°$.

velocities extending downward from near the ridge axis to the bottom of the isotropic models (Figure 10) has been greatly reduced or eliminated. Thus this feature is not demanded by the data when anisotropy is considered. The deepest extent of this central low-velocity anomaly is now ~200–300 km.

6.2.2. Fast Axis Dip

[46] Models with subridge anisotropic symmetry axes dipping at 0° or 30° to the west more closely fit the delay time and shear splitting data. This result is generally true irrespective of the dimensions of the subridge anisotropy

domain (Figure 11). The sensitivity of the delay time and shear wave splitting data to the dip of anisotropy increases with the volume of the subridge domain. Notably, the best fitting models have a subridge anisotropy domain that is 80 km deep or less, or has the fast axis oriented horizontal or dipping 30° to the west. Because of the parameterization of the subridge domain (Figure 6), when it is shallow, the flank anisotropy fills the space beneath it to a depth of 200 km. Thus both shallowness of the subridge domain or anisotropy that dips less than 30° to the west provide a greater volume of horizontally oriented fast axes. Either of these features is
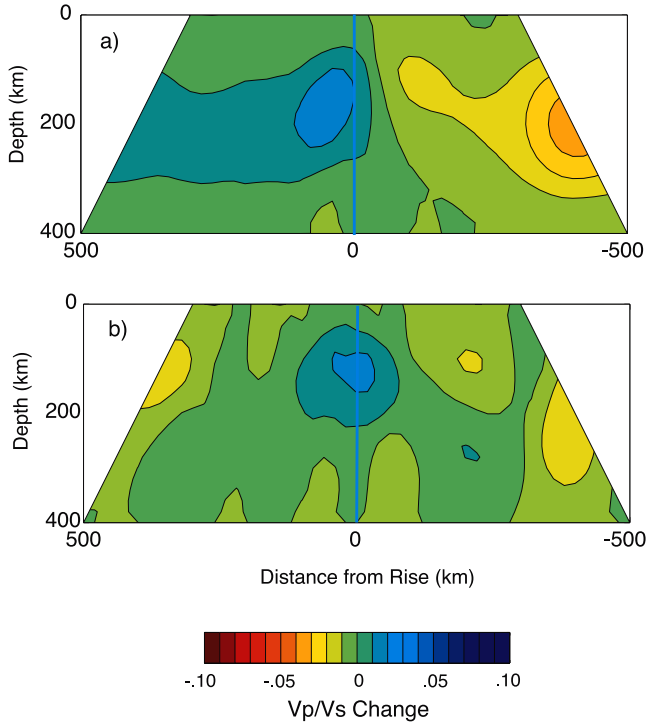
Figure 13. V_P/V_S for the first two models shown in Figure 11, where (a) V_P/V_S is smooth and (b) $\partial\ln V_S/\partial\ln V_P = 2.2$ everywhere.

effective at reducing the model misfit. From these inversions, we conclude that the body wave data are sensitive to the dip of anisotropy beneath the rise and, and that the presence of vertically oriented fast axes is limited in volume; given the crude domains that we have tested, the thickness would be less than 80 km.

6.2.3. Spatial Variation of $\partial\ln V_S/\partial\ln V_P$

[47] Holding $\partial\ln V_S/\partial\ln V_P$ constant results in increased data misfit, in comparison with models where $\partial\ln V_S/\partial\ln V_P$ is allowed to vary. Knowledge of $\partial\ln V_S/\partial\ln V_P$ is desirable because melt and temperature are expected to have different relative effects on P and S velocities [e.g., *Karato*, 1993; *Mavko*, 1980; *Schmeling*, 1985; *Hammond and Humphreys*, 2000], making this quantity diagnostic of the cause of a low-velocity perturbation. Fixing $\partial\ln V_S/\partial\ln V_P = 2.2$ results in χ_{tt}^2 from 6.0 to 8.1 (Figure 11b), significantly greater than models where the weaker constraint of smooth V_P/V_S is used (χ_{tt}^2 between 4.5 and 5.3). Fixing $\partial\ln V_S/\partial\ln V_P = 1.0$ gives results qualitatively similar to those of Figure 11b except that χ_{tt}^2 varies from 6.0 to 6.8. We conclude that the data require that $\partial\ln V_S/\partial\ln V_P$ to vary beneath the rise. For the model shown in Figures 12a and 12b, V_P/V_S is greater directly beneath the rise, and has east-west asymmetry with higher values west of the rise to a depth of 300 km. When $\partial\ln V_S/\partial\ln V_P = 2.2$ (Figures 12c and 12d) the elevated V_P/V_S is more symmetric (Figure 13). Because we use a damping constraint on the top row, V_P/V_S is not well constrained in the upper 40 km of these models, as discussed in section 6.2.4.

[48] A direct measurement of $\partial\ln V_S/\partial\ln V_P$ is difficult to obtain from our data since there are few arrival time anomalies for P and S waves for the same event. Thus we cannot use a δt_P versus δt_S slope fitting method [*Koper et*

al., 1999]. Furthermore, resolution of spatial variations in $\partial\ln V_S/\partial\ln V_P$ is sensitive to the details in the tomography and in our assumptions for the anisotropy model. However, we can conclude that models having $\partial\ln V_S/\partial\ln V_P = 2.2$ or 1.0 everywhere are inconsistent with the data.

6.2.4. Depth Extent of the Low V_P and V_S Anomaly

[49] The anomalously low seismic velocities extend to a depth of 200 to 300 km. The relationship between squeezing depth Z_S and the data misfit (Figure 14a) indicates that models having low velocities confined to the uppermost 100 km of the mantle fit the data significantly (to 95% confidence) worse that the models with $Z_S = 300$ or $Z_S = 400$. This result is invariant to the form of coupling between V_P and V_S and invariant to the presence of damping on the top row of the model (Figure 14a). Furthermore, in each of the models obtained in the grid search over anisotropic starting models,
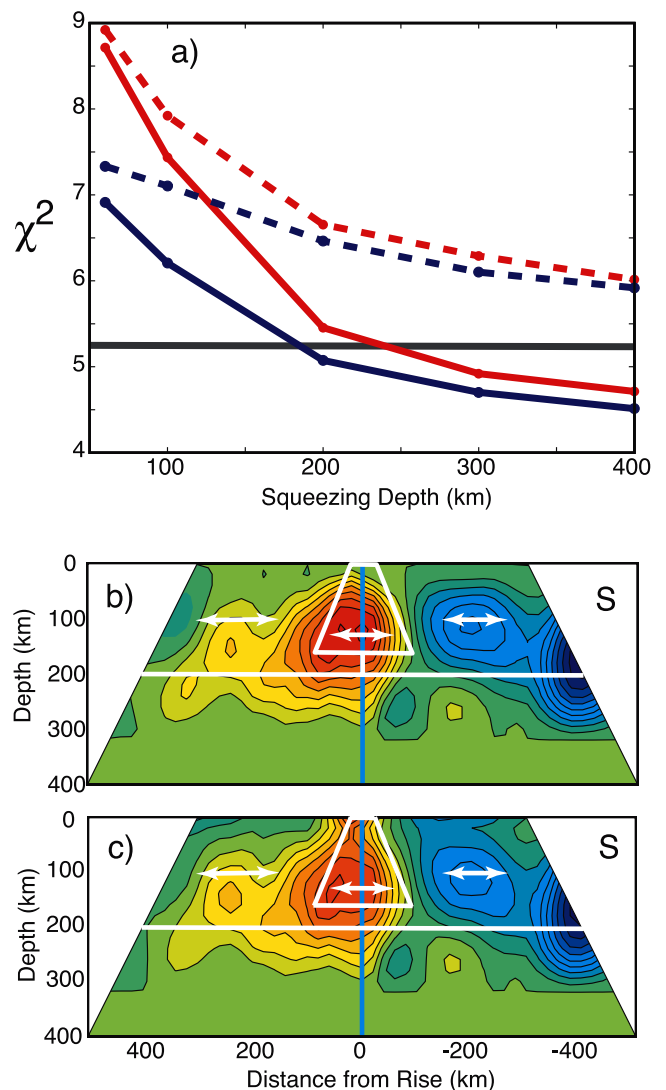

Figure 14. Effect of squeezing depth Z_S and top row damping on model misfit and inferred heterogeneity. Misfit as a function of Z_S (a) shown for models with smooth V_P/V_S (solid lines) and $\partial\ln V_S/\partial\ln V_P = 2.2$ (dotted lines), (b) for models with damping of the top row (red lines in Figure 14a), and (c) no damping on the top row (blue lines in Figure 14b). Color scale is the same as in Figure 12.

low velocities extend to 200–300 km depth, indicating that this result is invariant to the presence of the simple patterns of anisotropy that we test. Figure 14a suggests that the effect of changing Z_S on the data misfit is small when $Z_S > 300$ km, in accord with the results of the synthetic checkerboard test. This suggests that our choice of $Z_S = 400$ is sufficiently deep to include the structure causing the body wave delays. Damping of the top row has a small (insignificant to 95% confidence) effect on the data misfit when $Z_S > 300$ km. The effect of damping the top row on V_P and V_S heterogeneity is to inhibit the presence of low seismic velocities reaching up to the surface from the top of the primary low-velocity anomaly (shown for VS in Figures 14b and 14c). This feature is not required or excluded by the data. The effect of the additional damping of the top row is otherwise unnoticable in the V_P and V_S inferred heterogeneity.

7.   Discussion
7.1.   Physical State of the SEPR Upper Mantle

[50]   The tomographic images include an isotropic velocity anomaly that allows us to constrain variations in temperature and melt fraction beneath the SEPR. In so doing, we assume that compositional variations do not give rise to significant velocity anomalies [*Jordan*, 1979] and that melt and temperature provide isotropic velocity anomalies. Our approach is to predict seismic velocity anomalies for a range of possible melt and temperature anomalies by using relations between melt, temperature, and seismic velocity variation. We then evaluate the misfit between the observed velocity variation and that predicted by these relations to estimate the most likely physical state of the SEPR upper mantle. Quantitative estimation of the likelihood of this state is problematic, however. Explicit evaluation of the uncertainties requires knowledge of the variance of the velocity anomalies owing to tomographic uncertainty and to variance in the relations used to predict melt and temperature. The latter are difficult to estimate, owing to uncertainty in mantle activation enthalpy, geometry of melt containment, the physics of wave propagation through partially molten media, ambient mantle geotherm and Q. Here we provide estimates using available relations, and explore the sensitivity of the predictions to variation in upper mantle properties.

[51]   The effect of temperature variation on seismic wave velocity is the sum of anelastic (frequency-dependent and attenuating) and anharmonic (frequency-independent and nonattenuating) mechanisms for reduction in elastic modulus. The magnitude of these effects are dependent on the absolute temperature, the frequency of wave propagation, and the attenuation factor Q^{-1} [*Karato*, 1993]. Melt is expected to provide seismic velocity reduction to a degree sensitive to the melt fraction and geometry of melt containment [*Hammond and Humphreys*, 2000]. The lower density of the melt has relatively little effect on seismic velocity and is not considered here. Combining these effects linearly gives the total velocity reduction

$$\frac{\Delta V_P}{V_P} = \int_{T_0}^{T} \frac{\partial \ln V_P}{\partial \tau} d\tau + \int_{0}^{F} \frac{\partial \ln V_P}{\partial \phi} d\phi \qquad (29)$$

$$\frac{\Delta V_S}{V_S} = \int_{T_0}^{T} \frac{\partial \ln V_S}{\partial \tau} d\tau + \int_{0}^{F} \frac{\partial \ln V_S}{\partial \phi} d\phi \qquad (30)$$

valid for small F, where F is the melt fraction, T is the temperature in Celsius, and T_0 is a reference temperature. We use τ for temperature and ϕ for melt fraction in the integration. Provided with knowledge of T, F and their partial derivatives, we can use equations (29) and (30) to predict the change in V_P and V_S with respect to melt free mantle at temperature T_0. We calculate $\Delta V_P/V_P$ and $\Delta V_S/V_S$ with T of 1200 to 1450 C and F of 0 to 2.0%. We begin with $T_0 = 1300$ C, and use the relationships for $\partial \ln V_P/\partial T$ and $\partial \ln V_S/\partial T$ from equation (6) of *Karato* [1993]. For this we require values for Q_P and Q_S, and use

$$Q_S = 1.6 \times 10^3 e^{-3.466 \times 10^{-3} T}, \qquad (31)$$

obtained from *Jackson et al.* [1992]. We estimate Q_P from Q_S using

$$Q_P = \frac{3}{4} \left(\frac{V_P}{V_S} \right)^2 Q_S \qquad (32)$$

[*Anderson*, 1989]. The anharmonic derivatives have weak dependence on temperature, so we hold them fixed in this calculation [*Isaac*, 1992]. For melt, we use $\partial \ln V_P/\partial F = 3.6$ and $\partial \ln V_S/\partial F = 7.9$ for cuspate melt films occupying planar two-grain boundaries [*Faul et al.*, 1994; *Hammond and Humphreys*, 2000].

[52]   We compare these results to the tomographically determined values, and evaluate the misfit. The maximum horizontal percent velocity variations in our preferred V_P and V_S models (Figures 12a and 12b) occurs at 100–120 km depth and are $\Delta V_P/V_P = 1.9\%$ and $\Delta V_S/V_S = 2.7\%$, taken from within ± 300 km of the rise. For each temperature and melt fraction the misfit between the predicted and tomographically observed velocity variation is

$$E(F, T) = \sqrt{\left(\frac{\delta V_{P\%}}{\sigma_{P\%}} \right)^2 + \left(\frac{\delta V_{S\%}}{\sigma_{S\%}} \right)^2} \qquad (33)$$

where

$$\delta V_{P\%} = \frac{\Delta V_P}{V_P}\bigg|_{\text{observed}} - \frac{\Delta V_P}{V_P}\bigg|_{\text{calculated}} \qquad (34)$$

$$\delta V_{S\%} = \frac{\Delta V_S}{V_S}\bigg|_{\text{observed}} - \frac{\Delta V_S}{V_S}\bigg|_{\text{calculated}}, \qquad (35)$$

where $\sigma_{P\%}$ and $\sigma_{S\%}$ are scaled so that V_P and V_S have equal contribution, and so that the maximum E is normalized to one.

[53]   The results, for $T_0 = 1300°C$ (Figure 15a), illustrate the trade-off between melt and temperature variations. If temperature variations are assumed to be zero then $T = T_0$, a condition we might expect if upwelling is passive and purely adiabatic. In this case a melt fraction from 0.1% to 0.7% best explains the V_P and V_S perturbations. If the melt fraction is assumed to be zero, then the temperature most likely explaining the velocity variation is between 1310 and 1375°C, representing a temperature variation of 10 to 75°C. In Figure 15b the misfit estimates are repeated using $T_0 =$
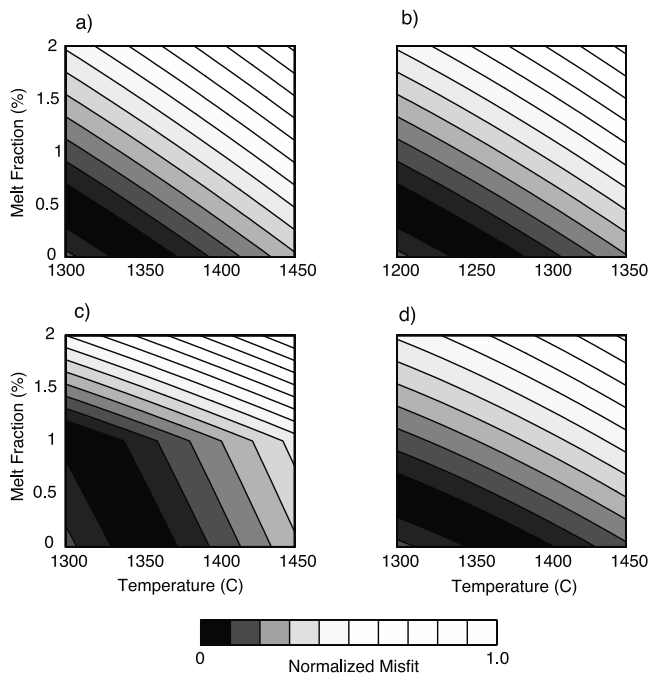
Figure 15. Contoured misfit of melt fraction and temperature to the tomographic models. The best fitting 25% of the tomographic models with smooth $\partial \ln V_S / \partial \ln V_P$ are compared to each temperature and melt fraction anomaly in the grid. (a) $T_0 = 1300$ K, (b) $T_0 = 1200$ K, (c) $T_0 = 1300$ K and melt is assumed to reside in tube shaped pores below $F = 1\%$, (d) $T_0 = 1300$ K but values for Q as a function of temperature are doubled compared to Figure 15a and equation (31).

1200°C. In this case the temperature change required to explain the seismic velocity variation has increased to between 25 and 90°C. We also test the effect of a change in melt containment geometry to three-grain junction tubules below $F = 1.0\%$ [*Waff and Bulau*, 1979] and films above $F = 1.0\%$ [*Faul et al.*, 1994] (Figure 15c). This primarily increases the estimate of melt fraction to approximately $F = 0.2\%$ to $F = 1.2\%$. We note that the relationship (31) predicts high maximum attenuation ($Q_P = 24$ and $Q_S = 11$) for the assumed reference temperatures. If experimental samples used to obtain equation (31) underestimate Q_S owing to differences between laboratory samples and mantle rocks, then the inferred temperature variations will be greater than those in Figures 15a–15c. We explore the sensitivity of the temperature estimate to background attenuation by doubling Q in our calculation. The estimated temperature change increases to between 40 and 100°C (Figure 15d). Thus the estimate of temperature variation is sensitive to the relationship between temperature and Q.

[54] These estimates apply to the maximum peak-to-peak variation in seismic velocity, which are subject to resolution issues. Tomography tends to spread velocity anomalies over larger volumes than they occupy, smooth their structure, and reduce their amplitude. Furthermore, the magnitude of the V_S anomaly varies somewhat with the applied V_P to V_S constraint. Thus, while we have provided estimates of temperature and melt content with the best relations available, the variances in our estimates (e.g., the width of the

darkest region in Figure 15) are necessarily subjective. Uncertainty in the depth of the maximum peak-to-peak velocity variation (100–120 km) is no exception. This depth is greater than the expected primary melt production region (less than ∼70 km) for mid-ocean ridge basalts, as inferred from their composition and geochemical models for melt segregation [e.g., *Hess*, 1992]. The depth of the inferred low seismic velocities, however, is not sensitive to our applied damping at the top of model (Figure 14), or to the squeezing depth when $Z_S > 300$. While some vertical smearing may have occurred it is unlikely that the low velocities are limited to the upper 100 km (Figure 14).

[55] Further constraints on the relative importance of temperature and melt to the seismic velocity anomalies may be obtainable by modeling mantle flow and heat transfer. The relatively strong horizontal gradients in the velocity structure, such as those seen in Figure 14b at depths of 100–200 km and between 25 and 100 km east of the rise, suggest a lateral transition in the amount of melt present. The temperature anomaly required to generate such a gradient is not likely to be supported on geologic time-scales. Consistent with this view, modeling of SEPR mantle flow shows that the observed east-to-west asymmetry in mantle temperature occurs over much greater length scales [*Toomey et al.*, 2002]. These results in combination with the variations in V_P/V_S reported here suggest that some combination of melt and temperature variation cause the observed seismic velocity variation.

7.2. Mantle Flow Beneath the SEPR

[56] The orientation of seismic anisotropy beneath the SEPR is diagnostic of the pattern of flow in the upper mantle. We have used a block parameterization to approximate the anisotropy as horizontal or dipping shallowly to the west. Because large shear strains tend to align the seismically faster olivine a axes approximately parallel to flow lines [*Ribe*, 1992], we use our simplistic estimate of anisotropy to infer a low-resolution picture of the flow direction beneath the SEPR. This picture allows distinction between first-order models of the subridge flow in large volumes of the mantle beneath the ridge.

[57] Our results are most consistent with a relatively shallow flow pattern, with asthenosphere ascending from beneath the western flank of the SEPR. Competing models for the pattern of mantle flow have different depths for the origin of the asthenosphere beneath the rise, and different dip angles for the ascending flow lines (Figures 16a–16c). These numerical flow models, shown in the reference frame of the migrating SEPR, use the MELT region plate kinematics at the surface, and include the effects of pressure and temperature dependence on viscosity [*Toomey et al.*, 2002]. They show that the westward ridge migration causes a westward dip of flow lines in the upwelling region (Figure 16a versus 16b). The depth of origin of the entrained asthenosphere is strongly dependent on the depth dependence of viscosity (Figure 16b versus 16c). Viscosity that increases more quickly with depth will promote a shallower asthenospheric return flow. Additionally, east-to-west cross-axis asymmetries in temperature and pressure can provide changes in the flow field that effect the orientation of streamlines [*Conder et al.*, 2002] and hence the dip of the anisotropy. Comparison of the dip of anisotropy preferred
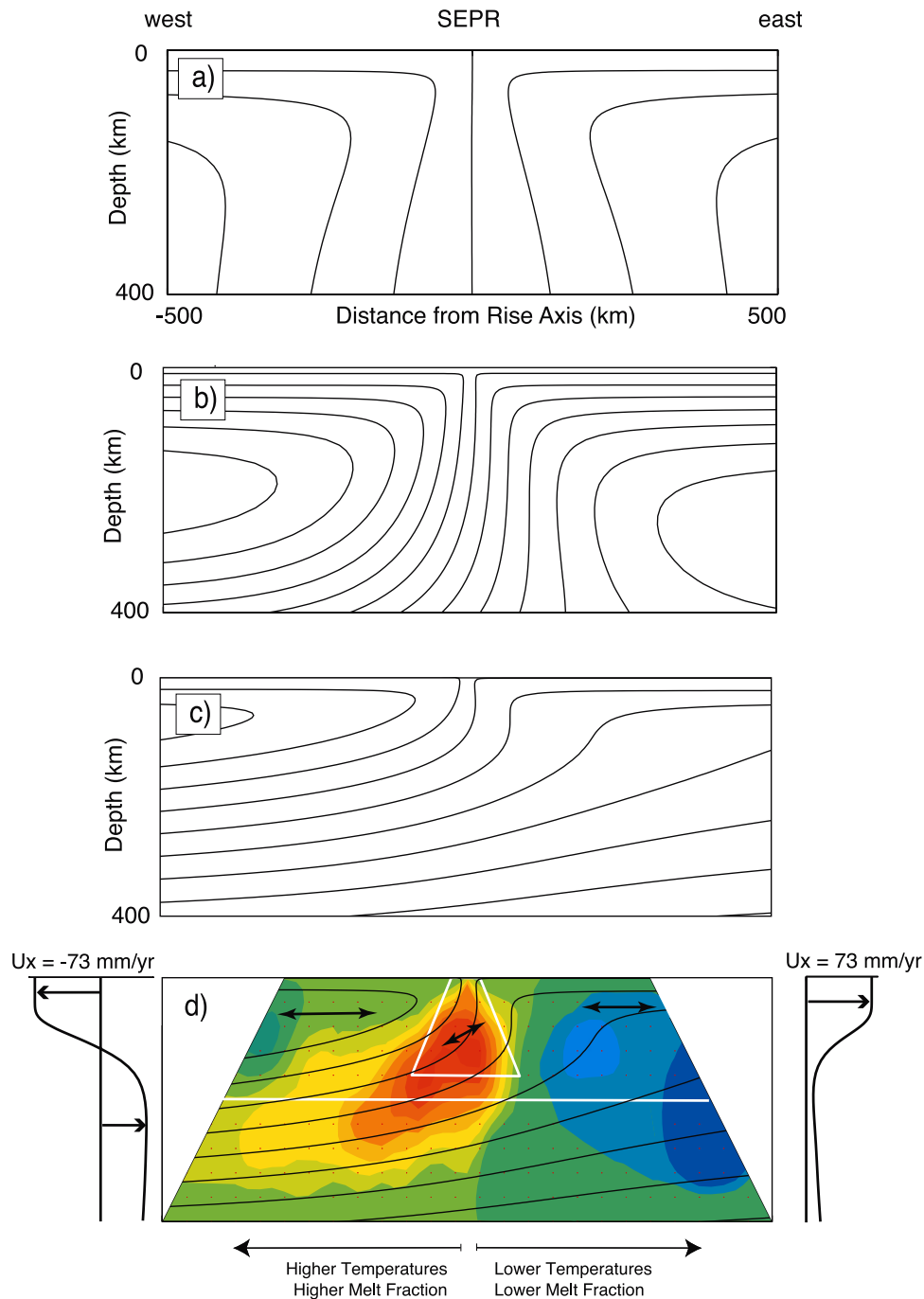
Figure 16. Numerically calculated flow lines for (a) symmetric plate spreading with a nearly isoviscous upper mantle, (b) asymmetric spreading owing to the SEPR migrating westward at 32 mm/yr, with nearly isoviscous upper mantle, (c) same as Figure 16b except that relative viscosity increases by about 2 orders of magnitude between the asthenosphere and the transition zone (see *Toomey et al.* [2002] for details). (d) Preferred V_S model (shown with flow lines from Figure 16c) (thin black lines) superimposed. Two-headed black arrows indicate the orientation of seismic anisotropy (fast axis for *P* waves). White lines indicate boundaries between anisotropy domains. Left (right) of contoured V_S is the depth dependence of horizontal component of mantle flow velocity U_x at the west (east) boundary, illustrating the influx of material from the western asthenosphere. Color scale is the same as in Figure 11.

by the MELT data to subaxis flow lines in Figure 16 suggests that a shallower return flow from the west is most compatible (as in Figure 16c). This suggestion is compatible with the weaker azimuthal anisotropy near the SEPR

rise axis inferred from Rayleigh waves [*Forsyth et al.*, 1998]. Other more complicated mantle flow patterns may be consistent with the data as long as the fast axes are predominantly horizontal in the vicinity of the white out-

lined block in Figure 16d. The anisotropy is not consistent with flow patterns that would result in large (>80 km wide or >80 km deep) regions of near vertically oriented fast axes.

7.3. Dynamics and Seismic Velocity Beneath the SEPR

[58] The results of this study suggest a passive flow regime beneath the SEPR. The lack of deep (>80 km) vertically oriented anisotropy in addition to the presence of a broad distribution (>200 km) of anomalously low seismic velocities are more similar to the predictions of passive flow models [*Turcotte and Phipps Morgan*, 1992; *Buck and Su*, 1989; *Su and Buck*, 1991]. Modeling by *Hung et al.* [2000] using the MELT S wave data further show that a narrow column of low seismic velocity is limited to be <5 km wide if it is 0.5 km/s slower than the ambient mantle. While it may be possible that a narrow column of upwelling partially molten mantle resides inside this width, the presence of the broader zone of low seismic velocities makes this unlikely. Furthermore, in a recent study of surface waves observed in the MELT experiment, the zone of lowest velocities gets progressively wider with depth starting directly beneath the Moho [*Dunn and Forsyth*, 2001], also consistent with a broader zone of melt generation in the subridge mantle.

[59] The depth extent of the lowest seismic velocities (to at least 200 km depth) are at odds with expectations from petrochemical models of mid-ocean ridge basalt (MORB) formation. These models state that the source region of MORB extends to not much more than 70 km depth [e.g., *Hess*, 1992]. Our seismic observations can be reconciled with these petrologic models if melt exists in small fractions (<1%) in unconnected pore spaces below 70 km. Very low permeability may prohibit melt below this depth from participating in the formation of MORB. At depths of 100–200 km, there is a lack of correlation between the regions of low seismic velocity and regions where there is an upward component mantle flow (black lines in Figure 16d). This may possibly be explained by the simplicity of the mantle flow models used here. Alternatively, the presence of higher temperatures in the mantle west of the rise may be the cause.

[60] The proximity of the South Pacific superswell to the west of the MELT region suggests the possibility that elevated temperatures and lower viscosities on the western side of the SEPR are the result of hot spot-fed asthenosphere. This hypothesis [*Phipps Morgan et al.*, 1995] explains the east-to-west asymmetry in low seismic velocities owing to greater amounts of melt and temperature, in addition to the orientation of anisotropy we have detected [*Toomey et al.*, 2002]. This interpretation of shallow return flow is also consistent with the lack of deflection in upper mantle discontinuities [*Shen et al.*, 1998], the asymmetry of shear wave splitting [*Wolfe and Solomon*, 1998], smaller subsidence rates and enhanced seamount population on the Pacific plate, and asymmetry in the mantle Bouguer anomaly [*Scheirer et al.*, 1998]. A detailed modeling study by *Toomey et al.* [2002] has shown that ridge migration itself is insufficient to induce east-west asymmetry in melt production. Thus the observations require some other source of asymmetry like temperature and/or pressure originating from the west, further suggesting an extra ridge

influence such as the South Pacific Superswell on the SEPR mantle.

8. Conclusions

[61] We have tomographically imaged seismic velocity heterogeneity and anisotropy beneath the southern East Pacific Rise using body wave delays and shear wave splitting measurements from the MELT experiment. We have shown that the P and S body wave delays are sensitive to the orientation of the anisotropic symmetry axis and that the heterogeneity inferred from the delay times is sensitive to the pattern of anisotropy.

[62] The magnitude of peak-to-peak velocity anomalies is greatest at a depth of 100–120 km, and are $\Delta V_P/V_P =$ 1.9% and $\Delta V_S/V_S = 2.7\%$ within 300 km of the rise. Melt fractions inferred from these seismic velocity perturbations are most likely less than 1.2%. Melt fractions as small as 0.3% can explain the velocity anomalies if the melt is contained in cuspate films for all melt fractions. If all velocity perturbation is the result of temperature variations beneath the MELT array, then ΔT is between 10 and 100°C, depending on the temperature assumed as a reference value and on the relationship between temperature and attenuation.

[63] After the addition of seismic anisotropy to the tomographic modeling, the seismic velocity anomalies have less east-to-west asymmetry. Significant asymmetry is, however, still inferred, with lower velocities beneath the Pacific plate.

[64] The most likely orientation of the anisotropic hexagonal symmetry axis beneath the ridge is horizontal or dipping roughly 30° to the west. An implication of this orientation of anisotropy is that the flow lines in the mantle beneath the SEPR are close to horizontal or dipping shallowly to the west. Vertical flow in the dislocation creep regime associated with upwelling is limited to a region <80 km deep.

Appendix A: Elastic Tensor

[65] Constraints on the form of an elastic tensor representing the anisotropy of the SEPR upper mantle come from observations of natural samples [*Peselnic and Nicolas*, 1978; *Christensen*, 1984; *Mainprice and Silver*, 1993; *Kern*, 1993], modeling of rock textures from shear deformation [*Ribe*, 1989; *Wenk et al.*, 1991; *Ribe and Yu*, 1991], modeling of rock elastic properties from petrophysical data [*Mainprice*, 1997] and observation of the seismic anisotropy from shear wave splitting [e.g., *Silver and Chan*, 1991; *Fischer and Wiens*, 1996; *Wolfe and Solomon*, 1998; *Schutt et al.*, 1998; *Savage*, 1999]. We have chosen an hexagonally symmetric tensor because it can reproduce the important features of the observed shear wave splitting. Furthermore, it is the simplest extension from isotropic, introducing the minimum number of additional free parameters needed to solve for the anisotropy and its orientation. When the hexagonal symmetry axis lies in the vertical plane normal to the rise, the S wave for the polarization parallel to the ridge arrives later, and hexagonal symmetry provides an approximately $\cos(2\alpha)$ dependence for the P and slow S wave. Figure A1 shows the directional dependence of the P and the two S wave polarizations. Progressive simple shear of peridotite tends to align the olivine a axis (seismically
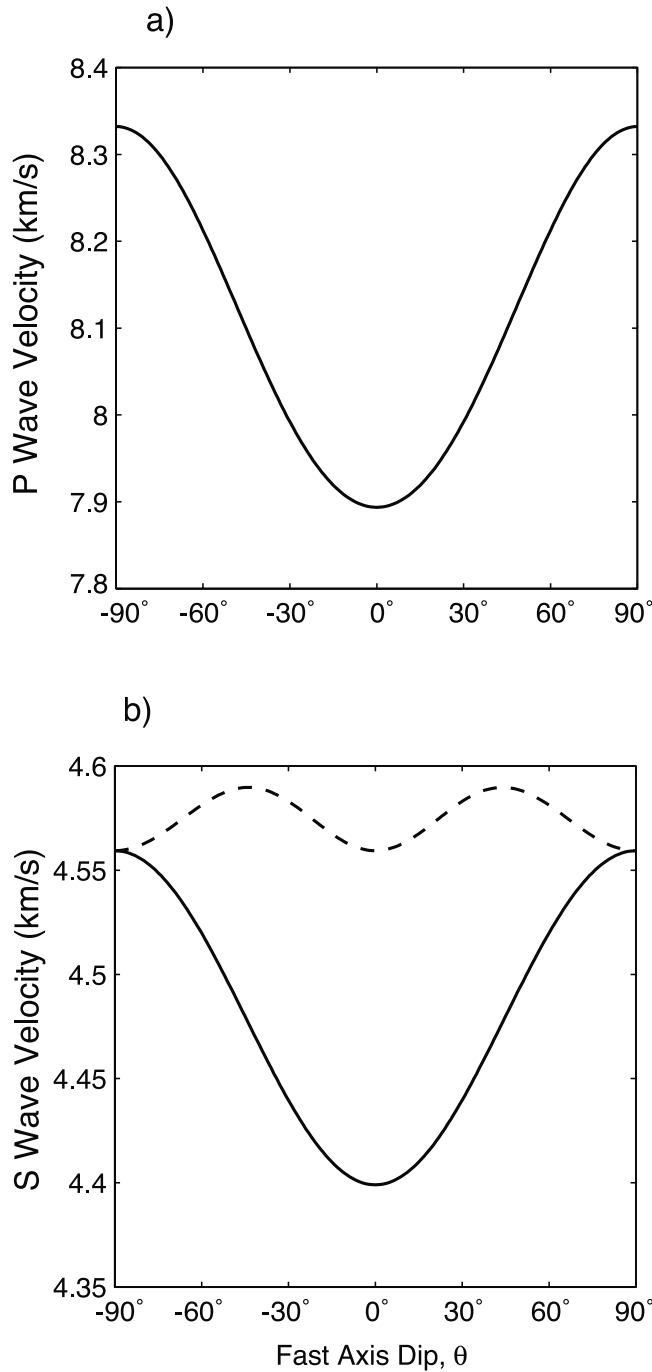
a)

b)

Figure A1. Seismic velocity in an hexagonally symmetric medium. Variation of (a) V_P and (b) V_S with dip of the hexagonal symmetry axis. Velocity shown is for a vertical ray path through a medium with the fastest V_P propagation direction dipping in the vertical plane normal to SEPR. In Figure A1b the solid line is for the slow S wave polarization, while the dashed line is for the fast S polarization. Note the similarity in form between the slow S wave and the P wave dependence on fast axis orientation.

fastest) in the direction of the shear, inside the foliation plane, and the b axis (slowest) normal to that plane. Given the orientation of shear strain in a two-dimensional flow field, we expect the mean a axis orientation to be inside the

vertical plane normal to the rise (Figure 6) [*Nishimura and Forsyth*, 1989; *Blackman et al.*, 1996].

[66] A tensor that has all of the required properties is shown in Table 2. This tensor is derived from laboratory measurements of ultrasonic seismic velocities in Ivrea zone peridotite at 600 MPa and 873 K [*Kern*, 1993]. Velocities were converted to elastic moduli by the formulas

$$c_{1111} = \rho V_{P1}^2 \tag{A1}$$

$$c_{2222} = \rho V_{P2}^2 \tag{A2}$$

$$c_{3333} = \rho V_{P2}^2 \tag{A3}$$

$$c_{2323} = \rho V_{S1}^2 \tag{A4}$$

$$c_{1313} = \rho V_{S2}^2 \tag{A5}$$

$$c_{1212} = \rho V_{S2}^2 \tag{A6}$$

$$c_{1122} = c_{2222} - 2c_{2323} \tag{A7}$$

$$c_{2233} = c_{2222} - 2c_{2323} \tag{A8}$$

$$c_{1133} = c_{2222} - 2c_{2323} \tag{A9}$$

and $c_{iijj} = c_{jjii}$, where V_{P1} is the fastest of the P velocities, V_{P2} is the average of the middle and slowest P velocities, V_{S1} is the average of the slowest shear velocity measurements, and V_{S2} is the average of the two fastest shear velocity measurements [*Babuska and Cara*, 1991]. In this hexagonal tensor, we have made the additional simplifying assumption that all off-diagonal terms in c_{iijj} for $1 \leq i, j \leq 3$ and $i \neq j$, are equal. In Table 2 we use the abbreviated tensor form C_{ij} so that $C_{11} = c_{1111}$, $C_{22} = c_{2222}$, $C_{33} = c_{3333}$, $C_{44} = c_{2323}$, $C_{55} = c_{1313}$, $C_{66} = c_{1212}$, and $C_{ij} = c_{iijj}$ for $i \neq j$ and $i \leq 3$ and $j \leq 3$.

[67] The directional dependence of velocity can be derived directly from this tensor by calculating the Christoffel matrix **M** whose elements are

$$m_{il} = \frac{c_{ijkl} n_j n_k}{\rho}, \tag{A10}$$

where ρ is the density of the rock and **n** is the unit vector in the direction of wave propagation. Einstein summation notation over indices j and k is implied. The eigenvalues of **M** are the squares of the phase velocities of waves traveling in the direction **n** [*Babuska and Cara*, 1991].

References

Anderson, D. L., *Theory of the Earth*, 366 pp., Blackwell Sci., Malden, Mass., 1989.

Babuska, V., and M. Cara, *Seismic Anisotropy in the Earth*, 217 pp., Kluwer Acad., Norwell, Mass., 1991.

Backus, G. E., Possible forms of seismic anisotropy of the uppermost mantle under oceans, *J. Geophys. Res.*, 70, 3429–3439, 1965.

Blackman, D. K., and J.-M. Kendall, Sensitivity of teleseismic body waves to mineral texture and melt in the mantle beneath a mid-ocean ridge, *Philos. Trans. R. Soc. London, Ser. A*, 355, 217–231, 1997.

Blackman, D. L., J. A. Orcutt, and D. W. Forsyth, Recording teleseismic earthquakes using ocean-bottom seismographs at mid-ocean ridges, *Bull. Seismol. Soc. Am.*, 85, 1648–1664, 1995.

Blackman, D. L., J.-M. Kendall, P. R. Dawson, H. R. Wenk, D. Boyce, and J. Phipps Morgan, Teleseismic imaging of sub-axial flow at mid-ocean ridges: Traveltime effects of anisotropic mineral texture in the mantle, *Geophys. J. Int.*, 127, 415–426, 1996.

Buck, W. R., and W. Su, Focussed mantle upwelling below mid-ocean ridges due to feedback between viscosity and melting, *Geophys. Res. Lett.*, 16, 641–644, 1989.

Canales, J. P., R. S. Detrick, S. Bazin, A. J. Harding, and J. A. Orcutt, Off-axis thickness across and along the East Pacific Rise within the MELT area, *Science*, 280, 1218–1221, 1998.

Christensen, N. I., The magnitude, symmetry and origin of upper mantle anisotropy based on fabric analysis of ultramafic tectonites, *Geophys. J. R. Astron. Soc.*, 76, 89–111, 1984.

Cochran, J. R., Variations in subsidence rates along intermediate and fast spreading mid-ocean ridges, *Geophys. J. R. Astron. Soc.*, 87, 421–454, 1986.

Conder, J. A., D. W. Forsyth, and E. M. Parmentier, Asthenospheric flow and the asymmetry of the East Pacific Rise, MELT area, *J. Geophys. Res.*, 107(B12), 2344, doi:10.1029/2001JB000807, 2002.

Dijkstra, E. W., A note on two problems in connection with graphs, *Numer. Math.*, 1, 269–271, 1959.

Dunn, R. A., and D. W. Forsyth, Short-period Love waves reveal the transition from broad mantle upwelling to the narrow crustal magmatic system beneath the southern East Pacific Rise, *Eos Trans. American Geophysical Union*, 82(47), Fall Meet. Suppl., Abstract T12A-0898, 2001.

Dunn, R. A., and D. R. Toomey, Seismological evidence for three-dimensional melt migration beneath the East Pacific Rise, *Nature*, 388, 259–262, 1997.

Dziewonski, A. M., and D. L. Anderson, Preliminary reference Earth model, *Phys. Earth Planet. Inter.*, 25, 297–356, 1981.

Ekström, G., and A. M. Dziewonski, The unique anisotropy of the Pacific upper mantle, *Nature*, 394, 168–172, 1998.

Evans, R. L., et al., Asymmetric electrical structure in the mantle beneath the East Pacific Rise at 17°S, *Science*, 286, 752–756, 1999.

Faul, U. H., D. R. Toomey, and H. S. Waff, Intergranular basaltic melt is distributed in thin, elongated inclusions, *Geophys. Res. Lett.*, 21, 29–32, 1994.

Fischer, K. M., and D. A. Wiens, The depth distribution of mantle anisotropy beneath the Tonga subduction zone, *Earth Planet. Sci. Lett.*, 142, 253–260, 1996.

Forsyth, D. W., The early structural evolution and anisotropy of the oceanic upper mantle, *Geophys. J. R. Astron. Soc.*, 43, 103–162, 1975.

Forsyth, D. W., S. C. Webb, L. M. Dorman, and Y. Shen, Phase velocities of Rayleigh waves in the MELT experiment of the East Pacific Rise, *Science*, 280, 1235–1238, 1998.

Hammond, W. C., Dynamics, flow and melt content of the Southern East Pacific Rise upper mantle from teleseismic tomography, Ph.D. thesis, 151 pp., Univ. of Oreg., Eugene, Dec. 2000.

Hammond, W. C., and E. D. Humphreys, Upper mantle seismic wave velocity: Effects of realistic partial melt geometries, *J. Geophys. Res.*, 105, 10,975–10,986, 2000.

Hess, H., Seismic anisotropy of the uppermost mantle under oceans, *Nature*, 203, 629–631, 1964.

Hess, P. C., Phase equilibria constraints on the origin of ocean floor basalts, in *Mantle Flow and Melt Generation at Mid-Ocean Ridges, Geophys. Monogr. Ser.*, vol. 71, edited by J. Phipps Morgan, D. K. Blackman, and J. M. Sinton, pp. 155–182, AGU, Washington, D. C., 1992.

Hung, S-.H., D. W. Forsyth, and D. R. Toomey, Can a narrow, melt-rich, low-velocity zone of mantle upwelling be hidden beneath the East Pacific Rise? Limits from waveform modeling and the MELT Experiment, *J. Geophys. Res.*, 105, 7945–7960, 2000.

Isaac, D. G., High-temperature elasticity of iron-bearing olivines, *J. Geophys. Res.*, 97, 1871–1885, 1992.

Jackson, D. D., The use of a priori data to resolve non-uniqueness in linear inversion, *Geophys. J. R. Astron. Soc.*, 57, 137–157, 1979.

Jackson, I. M., M. S. Paterson, and J. D. FitzGerald, Seismic wave dispersion and attenuation in dunite: An experimental study, *Geophys. J. Int.*, 108, 517–534, 1992.

Jordan, T. H., Mineralogies, densities and seismic velocities of garnet lherzolites and their geophysical implications, in *The Mantle Sample: Inclusions in Kimberlites and Other Volcanics: Proceedings of the Second International Kimberlite Conference*, vol. 2, edited by F. R. Boyd and H. O. A. Meyer, pp. 1–14, AGU, Washington, D. C., 1979.

Kaminski, E., and N. M. Ribe, A kinematic model for recrystallization and texture development in olivine polycrystals, *Earth Planet. Sci. Lett.*, 189, 253–267, 2001.

Karato, S., Importance of anelasticity in the interpretation of seismic tomography, *Geophys. Res. Lett.*, 20, 1623–1626, 1993.

Karato, S.-I., and P. Wu, Rheology of the upper mantle; a synthesis, *Science*, 260, 771–778, 1993.

Keen, C. E., and D. L. Barrett, A measurement of seismic anisotropy in the northeast Pacific, *Can. J. Earth Sci.*, 8, 1056–1064, 1971.

Kendall, J.-M., Teleseismic arrivals at a mid-ocean ridge: Effects of mantle melt and anisotropy, *Geophys. Res. Lett.*, 21, 301–304, 1994.

Kennet, B. L. N., and E. R. Engdahl, Traveltimes for global earthquake location and phase identification, *Geophys. J. R. Astron. Soc.*, 105, 429–465, 1991.

Kern, H., P- and S- wave anisotropy and shear-wave splitting at pressure and temperature in possible mantle rocks and their relation to the rock fabric, *Phys. Earth Planet. Inter.*, 78, 245–256, 1993.

Koper, K. D., D. A. Wiens, L. M. Dorman, J. Hildebrand, and S. C. Webb, Constraints on the origin of slab and mantle wedge anomalies in Tonga from the ratio of *S* to *P* velocities, *J. Geophys. Res.*, 104, 15,089–15,104, 1999.

Mainprice, D., Modeling the anisotropic seismic properties of partially molten rocks found at mid-ocean ridges, *Tectonophysics*, 279, 161–179, 1997.

Mainprice, D., and P. G. Silver, Interpretation of SKS-waves using samples from the subcontinental lithosphere, *Phys. Earth Planet. Inter.*, 78, 257–280, 1993.

Mavko, G. M., Velocity and attenuation in partially molten rocks, *J. Geophys. Res.*, 85, 5173–5189, 1980.

MELT Seismic Team, Imaging the deep seismic structure beneath a mid-ocean ridge: The MELT experiment, *Science*, 280, 1215–1218, 1998.

Montagner, J. P., and H. C. Nataf, On the inversion of the azimuthal anisotropy of surface waves, *J. Geophys. Res.*, 91, 511–520, 1986.

Moser, T. J., Shortest path calculation of seismic rays, *Geophysics*, 56, 59–67, 1991.

Nicolas, A., and N. I. Christensen, Formation of anisotropy in upper mantle peridotites; a review, in *Composition, Structure and Dynamics of the Lithosphere-Asthenosphere System, Geodyn. Ser.*, vol. 16, edited by K. Fuchs and C. Froidevaux, pp. 111–123, AGU, Washington, D. C., 1987.

Nishimura, C. E., and D. W. Forsyth, The anisotropic structure of the upper mantle in the Pacific, *Geophys. J. Int.*, 96, 203–229, 1989.

Paige, C. C., and M. A. Saunders, LSQR: An algorithm for sparse linear equations and sparse least squares, *ACM Trans. Math. Software*, 8, 43–71, 1982.

Parmentier, E. M., and J. Phipps Morgan, Spreading rate dependence of three-dimensional structure in oceanic spreading centers, *Nature*, 348, 325–328, 1990.

Peselnick, L., and A. Nicolas, Seismic anisotropy in an ophiolite peridotite: Application to oceanic upper mantle, *J. Geophys. Res.*, 83, 1227–1235, 1978.

Phipps Morgan, J., W. J. Morgan, Y.-S. Zhang, and W. H. F. Smith, Observational hints for a plume-fed, sub-oceanic asthenosphere and its role in mantle convection, *J. Geophys. Res.*, 100, 12,753–12,767, 1995.

Raitt, R. W., G. G. Shor Jr., T. J. G. Francis, and G. B. Morris, Anisotropy of the Pacific upper mantle, *J. Geophys. Res.*, 74, 3095–3109, 1969.

Ribe, N. M., Seismic anisotropy and mantle flow, *J. Geophys. Res.*, 97, 4213–4223, 1989.

Ribe, N. M., On the relation between seismic anisotropy and finite strain, *J. Geophys. Res.*, 97, 8737–8747, 1992.

Ribe, N. M., and Y. Yu, A theory for plastic deformation and textural evolution of olivine polycrystals, *J. Geophys. Res.*, 96, 8325–8335, 1991.

Sato, H., I. S. Sacks, T. Murase, and C. M. Scarfe, Thermal structure of the low velocity zone derived from laboratory and seismic investigations, *Geophys. Res. Lett.*, 15, 1227–1230, 1988.

Savage, M. K., Seismic anisotropy and mantle deformation: What have we learned from shear wave splitting?, *Rev. Geophys.*, 37, 65–106, 1999.

Scheirer, D. S., D. W. Forsyth, M.-H. Cormier, and K. C. Macdonald, Shipboard geophysical indications of asymmetry and melt production beneath the East Pacific Rise near the MELT experiment, *Science*, 280, 1221–1224, 1998.

Schmeling, H., Numerical models on the influence of partial melt on elastic, anelastic and electrical properties of rocks, part I, Elasticity and anelasticity, *Phys. Earth Planet. Inter.*, 41, 34–57, 1985.

Schutt, D., E. D. Humphreys, and K. G. Dueker, Anisotropy of the Yellowstone Hotspot wake, eastern Snake River Plane, Idaho, *Pure Appl. Geophys.*, 151, 443–462, 1998.

Scott, D. R., and D. J. Stevenson, A self-consistent model of melting, magma migration and buoyancy-driven circulation beneath mid-ocean ridges, *J. Geophys. Res.*, *94*, 2973–2988, 1989.

Shen, Y., A. F. Sheehan, K. G. Dueker, and H. Gilbert, Mantle discontinuity structure beneath the southern East Pacific Rise from *P*-to-*S* converted phases, *Science*, *280*, 1232–1234, 1998.

Silver, P. G., and W. W. Chan, Shear wave splitting and sub-continental mantle deformation, *J. Geophys. Res.*, *96*, 16,429–16,454, 1991.

Su, W., and W. R. Buck, Factors causing melt concentrations at mid-ocean ridges, *Eos Trans. American Geophysical Union*, *72*(17), Spring Meet. Suppl., 265, 1991.

Tarantola, A., and B. Valette, Inverse problems: Quest for information, *J. Geophys.*, *50*, 159–170, 1982.

Tommasi, A., Forward modeling of the development of seismic anisotropy in the upper mantle, *Earth Planet. Sci. Lett.*, *160*, 1–13, 1998.

Toomey, D. R., S. C. Solomon, and G. M. Purdy, Tomographic imaging of the shallow crustal structure of the East Pacific Rise at 9°30′N, *J. Geophys. Res.*, *99*, 24,135–24,157, 1994.

Toomey, D. R., W. S. D. Wilcock, S. C. Solomon, W. C. Hammond, and J. A. Orcutt, Mantle seismic structure beneath the MELT region of the East Pacific Rise from *P* and *S* tomography, *Science*, *280*, 1224–1227, 1998.

Toomey, D. R., W. S. D. Wilcock, J. A. Conder, D. W. Forsyth, J. D. Blundy, E. M. Parmentier, and W. C. Hammond, Asymmetric mantle dynamics in the MELT Region of the East Pacific Rise, *Earth Planet. Sci. Lett.*, *200*, 287–295, 2002.

Turcotte, D. L., and J. Phipps Morgan, The physics of magma migration and mantle flow beneath a mid-ocean ridge, in *Mantle Flow and Melt Generation at Mid-Ocean Ridges*, *Geophys. Monogr. Ser.*, vol. 71, edited by J. Phipps Morgan, D. K. Blackman, and J. M. Sinton, pp. 155–182, AGU, Washington, D. C., 1992.

VanDecar, J. C., and R. S. Crosson, Determination of teleseismic relative phase arrival times using multi-channel cross-correlation and least squares, *Bull. Seismol. Soc. Am.*, *80*, 150–169, 1990.

Waff, H. S., and J. R. Bulau, Equilibrium fluid distribution in ultramafic partial melt under hydrostatic stress conditions, *J. Geophys. Res.*, *84*, 6109–6114, 1979.

Webb, S. C., Broadband seismology and noise under the ocean, *Rev. Geophys.*, *36*, 105–142, 1998.

Wenk, H.-R., K. Bennett, G. R. Canova, and A. Molinari, Modeling plastic deformation of peridotite with the self-consistent theory, *J. Geophys. Res.*, *96*, 8337–8349, 1991.

Wessel, P., and W. H. F. Smith, New, improved version of the Generic Mapping Tools released, *Eos Trans. AGU*, *79*, 579, 1998.

Wiggins, R. A., The general linear inverse problem: Implication for surface waves and free oscillations for Earth structure, *Rev. Geophys.*, *10*, 251–285, 1972.

Wilcock, W. S. D., and S. C. Webb, The effect of local wind on seismic noise near 1 Hz at the MELT site and in Iceland, *Bull. Seismol. Soc. Am.*, *89*, 1543–1557, 1999.

Wolfe, C. J., and P. G. Silver, Seismic anisotropy of oceanic upper mantle: Shear wave splitting methodologies and observations, *J. Geophys. Res.*, *103*, 749–771, 1998.

Wolfe, C. J., and S. C. Solomon, Shear-wave splitting and implications for mantle flow beneath the MELT region of the East Pacific Rise, *Science*, *280*, 1230–1232, 1998.

Zhang, S., and S.-I. Karato, Lattice preferred orientation of olivine in simple shear deformation and the flow geometry of the upper mantle of the Earth, *Nature*, *375*, 774–777, 1995.

————————

W. C. Hammond, U.S. Geological Survey, 345 Middlefield Road, MS/977, Menlo Park, CA 94025, USA. (bhammond@usgs.gov)

D. R. Toomey, Department of Geological Sciences, University of Oregon, Eugene, OR 97403, USA. (drt@newberry.uoregon.edu)